Oncogenesis

https://doi.org/10.1038/s41389-026-00603-7

Article in Press

GPX3 suppresses gallbladder cancer progression by modulating redox balance, glycolysis, and anti-tumor immunity

Received: 29 August 2025

Revised: 13 January 2026

Accepted: 13 February 2026

Cite this article as: Ma, Z., Sun, J., Wu, X. *et al.* GPX3 suppresses gallbladder cancer progression by modulating redox balance, glycolysis, and anti-tumor immunity. *Oncogenesis* (2026). https://doi.org/10.1038/s41389-026-00603-7

Zuyi Ma, Jia Sun, Xin Wu, Changzhen Shang & Binglu Li

GPX3 Suppresses Gallbladder Cancer Progression by Modulating Redox Balance, Glycolysis, and Anti-Tumor Immunity

Running Title: GPX3 regulates metabolism and immunity in GBC

Zuyi Ma [1, 2, 3], Jia Sun [3], Xin Wu [3], Changzhen Shang [1,2*], Binglu Li [3*]

Author's Affiliations:

[1] Department of Hepatobiliary Surgery, Sun Yat-Sen Memorial Hospital, Guangzhou, Guangdong, China.

[2] Guangdong Provincial Key Laboratory of Malignant Tumor Epigenetics and Gene Regulation, Sun Yat-sen Memorial Hospital, Sun Yat-Sen University, Guangzhou, Guangdong, China.

[3] Department of General Surgery, State Key Laboratory of Complex Severe and Rare Diseases, Peking Union Medical College Hospital, Chinese Academy of Medical Science and Peking Union Medical College, Beijing, China.

Correspondence to:

Changzhen Shang, Department of Hepatobiliary Surgery, Sun Yat-Sen Memorial Hospital, No. 107, Yanjiang West Road, Yuexiu District, Guangzhou, Guangdong, China. **E-mail**: shchzh2@mail.sysu.edu.cn **Tel.:** +86-18510335286

Binglu Li, Department of General Surgery, State Key Laboratory of Complex Severe and Rare Diseases, Peking Union Medical College Hospital, Chinese Academy of Medical Science and

Peking Union Medical College, No. 1 Shuaifuyuan, Dongcheng District, Beijing, China. **E-mail**: PUMCHLBL@163.com **Tel.:** +86-13611161019

Abstract

Gallbladder cancer (GBC) is an aggressive malignancy characterized by metabolic plasticity and profound immune evasion. However, the functional role of glutathione peroxidase 3 (GPX3), a secreted antioxidant enzyme, in these processes remains unclear. Multi-omics analyses of paired GBC and adjacent non-tumor tissues revealed consistent downregulation of GPX3, which correlated with reactive oxygen species (ROS) accumulation and enhanced glycolytic activity. Functional restoration of GPX3 in GBC cells reduced intracellular ROS levels, suppressed the expression of glycolysis-related enzymes, and consequently impaired tumor proliferation, migration, and invasion. In xenograft models, GPX3 overexpression markedly attenuated tumor growth and lung metastasis. Notably, GPX3 restoration also enhanced $CD8^+$ T cell infiltration and elevated pro-inflammatory cytokine production, suggesting reversal of tumor-associated immunosuppression. These findings identify GPX3 as a critical tumor suppressor that integrates redox regulation, metabolic reprogramming, and immune activation to restrict malignant progression. Targeting GPX3 or its downstream pathways may represent a promising therapeutic strategy to simultaneously suppress gallbladder cancer aggressiveness and reinforce anti-tumor immunity.

Keywords: Gallbladder cancer, GPX3, Redox homeostasis, Glycolysis, Immune evasion, Metastasis

Introduction

The incidence and mortality rates of gallbladder cancer (GBC) are escalating annually [1, 2]. Oxidative stress and glycolysis play crucial roles in the development of GBC [3-5]. Studies indicate that the upregulation of oxidative stress and glycolysis processes may be associated with immune evasion and metastasis in GBC [3, 6, 7].

GPX3 is a key antioxidant gene that plays an important role in various cancers [8, 9]. However, in GBC, the expression level of GPX3 is significantly downregulated [10]. This downregulation may have an impact on oxidative stress and glycolysis in GBC, thereby influencing its development and metastasis [10].

Oxidative stress is a cellular stress response caused by accumulating intracellular oxidants [11, 12]. In GBC, oxidative stress can lead to enhanced proliferation, invasion, and metastatic abilities of GBC cells [13]. Glycolysis provides a key metabolic source of energy that supports the survival and growth of GBC cells [14-16]. Therefore, understanding the mechanisms of oxidative stress and glycolysis in GBC is essential for advancing mechanistic insight and guiding therapeutic development [3, 7, 17].

Previous studies have revealed a correlation between the downregulation of GPX3 and the occurrence and progression of GBC [10]. The decreased expression of GPX3 may promote immune evasion and metastasis in GBC by regulating oxidative stress and glycolysis processes [18, 19]. Nevertheless, how reduced GPX3 expression contributes to GBC pathogenesis remains insufficiently defined. Deeper investigation into its regulatory actions may uncover previously unrecognized mechanisms and highlight new therapeutic opportunities for GBC intervention [20, 21].

This study aims to investigate the impact of GPX3 expression changes on oxidative stress and glycolysis levels in GBC, and examines its contribution to immune escape and metastatic

progression. Clarifying the regulatory consequences of GPX3 downregulation on oxidative stress and glycolysis may reveal new molecular targets and inform therapeutic strategies for GBC management. The results are expected to advance understanding of GBC pathogenesis and provide a scientific foundation for developing more effective treatment options for patients.

Methods

Clinical Sample Collection

Clinical and pre-lesion gallbladder tissues were obtained from nine patients who underwent surgical treatment for GBC at our hospital between January and December 2023. As a non-tumorous control, tissue located 2 cm from the tumor margin was also collected. In addition, 20 mL of peripheral blood was drawn from healthy donors for T-cell isolation. None of the enrolled patients had received chemotherapy, radiotherapy, or other antitumor therapies prior to surgery, and all had no notable comorbidities (Supplementary Table 1). The excised tissues were immediately frozen in liquid nitrogen and preserved at −80 °C. All patients were informed about the study and provided written consent prior to surgery. The study was approved by the ethics committee of Peking Union Medical College Hospital, Chinese Academy of Medical Science and Peking Union Medical College (No. I-23PJ352) and all procedures complied with the principles of the Helsinki Declaration [22, 23].

High-throughput Transcriptome Sequencing of GBC Samples

Tumor tissues and matched adjacent non-tumorous tissues were obtained from three patients with GBC in each group. Total RNA was isolated using TRIzol reagent (ThermoFisher, 15596026, USA). RNA concentration, purity, and integrity were evaluated with a Qubit® 2.0 Fluorometer

(Life Technologies, Q33216, USA) and the Qubit® RNA Assay Kit (Shanghai Baoji Biotechnology, HKR2106-01, China), a NanoDrop spectrophotometer (IMPLEN, USA), and the RNA Nano 6000 Kit on the Agilent Bioanalyzer 2100 system (Agilent, 5067-1511, USA). For library construction, 3 μg of high-quality RNA from each sample served as input.

cDNA libraries were prepared using the NEBNext® UltraTM RNA Library Prep Kit for Illumina® platforms (NEB, E7435L, China), and library quality was confirmed on the Agilent Bioanalyzer 2100. Indexed libraries were clustered on a cBot system using the TruSeq PE Cluster Kit v3-cBot-HS (Illumina, PE-401-3001, USA) and subsequently sequenced on the Illumina HiSeq 550 platform to generate 125 bp/150 bp paired-end reads.

Raw sequencing data were assessed with FastQC v0.11.8. Adapter sequences and poly(A) tails were trimmed using Cutadapt 1.18. Reads containing >5% ambiguous bases were removed with Perl scripts, and high-quality reads (≥70% of bases with $Q \geq 20$) were retained using the FASTX Toolkit 0.0.13. Paired-end reads were repaired with BBMap, and the resulting clean reads were aligned to the human reference genome using HISAT2 (v0.7.12).

Subsequent analyses were performed using the Xiantao Academic bioinformatics platform. Differential gene expression was determined with the R package “limma,” applying the thresholds $|\log_2 FC| > 1$ and adjusted $P < 0.05$. Volcano plots and heatmaps were generated using ggplot2 and ComplexHeatmap. Principal component analysis (PCA), Gene Ontology (GO) enrichment, and Kyoto Encyclopedia of Genes and Genomes (KEGG) enrichment analyses were conducted and visualized with ggplot2. The GBC transcriptomic dataset GSE139682, containing ten GBC and ten normal samples, was downloaded from GEO (www.ncbi.nlm.nih.gov/geo/) and processed using the Weighted Gene Co-expression Network Analysis (WGCNA) package to identify both unique and shared transcriptional modules across groups. Venn diagrams were produced with the ggplot2 and VennDiagram packages [24, 25].

Protein Sequencing of GBC Samples

Tumor tissues, pre-lesion tissues, and adjacent normal tissue samples were collected from six GBC patients. Total protein was isolated using the Invitrogen protein extraction buffer (Invitrogen, 78501, USA), and protein concentrations were quantified with the BCA assay. Proteins were separated by gel electrophoresis and subsequently digested into peptides using trypsin (Invitrogen, 15400054, USA) under acidic conditions. After solid-phase extraction (SPE) to remove residual contaminants, peptide samples were analyzed by liquid chromatography–mass spectrometry (LC–MS).

The sequencing results were analyzed online using the bioinformatics tools available on the Xiantao Academic Online website. The "limma" package in R software was used for differential expression analysis of the dataset, with correction of the false discovery rate (FDR) for differential p-values. Differentially expressed proteins (DEPs) with $|\log2FC| > 0.5$ and $P.adjust < 0.05$ were selected. Volcano plots and heat maps were generated using the ggplot2 and ComplexHeatmap packages, respectively. PCA and GO/KEGG enrichment analysis were performed and visualized with ggplot2. Overlapping and unique DEPs across sample groups were further examined, and Venn diagrams were constructed using the VennDiagram package [26].

Metabolomics Analysis

Frozen tissue samples were thawed on ice, and an appropriate portion of each specimen was transferred to a pre-chilled mortar. Phosphate buffer was added to fully moisten the tissue, which was subsequently homogenized using a tissue disruptor to ensure complete mechanical lysis. The homogenate was transferred to a 1.5-mL polypropylene tube, mixed with 900 μL of 80% methanol containing 0.1% formic acid, vortexed for 2 min, and centrifuged at 12,000 × g for 10 minutes.

The resulting supernatant was collected and placed into autosampler vials for analysis.

Metabolomic profiling was performed using an LC20 ultra-high-performance liquid chromatography (UHPLC) system (Shimadzu, Japan) coupled to a Triple TOF 6600 mass spectrometer (AB Sciex). Chromatographic separation was achieved on a Waters ACQUITY UPLC HSS T3 C18 column (100 × 2.1 mm, 1.8 μm) maintained at 40 °C with a 0.4 mL/min flow rate. The mobile phase consisted of acetonitrile containing 0.1% formic acid, and the gradient for mobile phase B was programmed as follows: 5% from 0.0–11.0 min, increased to 90% between 11.0–12.0 min, and subsequently returned to 5% from 12.1–14.0 min. The eluent was delivered directly into the mass spectrometer without flow splitting.

Mass spectrometric acquisition was conducted under the following conditions: ionization voltage 5,500 V, capillary temperature 550 °C, nebulizing gas at 50 psi, and auxiliary gas at 60 psi. The metabolomics data were normalized using the MetaboAnalyst 5.0 database, and PCA analysis was performed for data dimensionality reduction. Metabolites with |Fold change| > 2 were selected using a T-test with a threshold of $P < 0.05$. The results of the Fold change and T-test analyses were combined to generate volcano plots and heatmaps.

To further evaluate the changes in metabolites, an orthogonal partial least squares–discriminant analysis (OPLS-DA) model was constructed, and score plots were generated. Based on the OPLS-DA results, metabolites were selected using the criterion VIP (Variable Importance in Projection) > 1 in the OPLS-DA S-plot and variable importance projection. The differentially regulated metabolites were identified by combining the results of log2FC, T-test, and OPLS-DA analyses, and a Venn diagram was used to determine the intersection. Enrichment analysis of the differentially regulated metabolites was performed using the KEGG and SMPDB databases [27, 28].

Construction of Lentivirus

Lentiviral vectors used in this study included the pSIH1-H1-copGFP short hairpin interference vector (System Biosciences, SI501A-1, USA) and the pCMV6-AC-GFP expression vector (LMAI Bio, LM-2069), which was employed for GPX3 overexpression. Lentiviral particles were produced in HEK-293T cells (iCell-h237; Saibaikang Biotechnology, Shanghai, China) using the Lentivirus Packaging Kit (Invitrogen, A35684CN, USA). After 48 hours of transfection, the supernatant containing packaged lentivirus particles was harvested, yielding a final viral titer of 1×10^8 TU/mL. The sequences for sh-NC and sh-GPX3 were as follows: sh-NC: ATTCGAGGCATCACTACAGAC, sh-GPX3-1: GTGGAGGCTTTGTCCCTAATT, sh-GPX3-2: GTGGCATAAGTGGCACCATTT, sh-GPX3-3: GCCTCCAAATATTAGTAACTA [29].

Cell Culture and Grouping

Human gallbladder epithelial cells HGBEC (Yimo Biotechnology, IM-H347), human GBC cells NOZ (Yimo Biotechnology, IM-H349), OCUG-1 cell line (Binsi Biotechnology, BS-C00668849S), human GBC cells SGC-996 (Mingzhou Biotechnology, MZ-1916), and EH-GB1 (Yaji Biotechnology, YS3570C) were cultured in DMEM medium (Wuhan Punose Life Science Co., Ltd., PM150210) containing 10% FBS. Human GBC cells GBC-SD (Wuhan Punose Life Science Co., Ltd., CL-0085) were cultured in RPMI-1640 medium containing 10% FBS. Based on experimental requirements, GBC-SD cells were divided into oe-NC and oe-GPX3 groups, while NOZ cells were divided into sh-NC and sh-GPX3 groups. Based on the sequence targeted by sh-GPX3-1, synonymous mutations were introduced into the GPX3 gene sequence using a site-directed mutagenesis strategy (see GPX3-MUT file). The mutated GPX3 gene fragment was then cloned into the pCMV6-AC-GFP vector (LM-2069, LMAI Bio) to generate the GPX3-MUT group, with pCMV6-AC-GFP (MUT-CON) serving as the control. The GPX3-MUT and MUT-CON

constructs were subsequently transfected into sh-GPX3 NOZ cells.

For lentiviral infection, 5×10^5 cells were seeded in six-well plates and exposed to packaged lentivirus (MOI = 10; working titer ~5×10^6 TU/mL) supplemented with 5 μg/mL polybrene (Merck, TR-1003, USA) once cultures reached ~50% confluence. After 4 hours, an equal volume of medium was added to dilute polybrene, followed by medium replacement at 24 hours. Infection efficiency was assessed at 48 hours using a luciferase reporter assay. Stable cell lines were generated via selection with 2 μg/mL puromycin (Gibco, A1113803, USA) for 7 days and validated by reverse transcription quantitative PCR (RT-qPCR).

For co-culture assays, peripheral blood from healthy donors was diluted 1:1 with saline, and mononuclear cells were isolated using FICOLL PAQUE PLUS (Yuningwei, 17144002-1). T cells were purified from peripheral blood mononuclear cells (PBMCs) with the Dynabeads™ Untouched™ Human T Cell Kit (Thermo Fisher, 11344D) and maintained in RPMI-1640 medium (Wuhan Punoise, PM150110) containing 10% fetal bovine serum (FBS). Purified T cells were seeded in the upper chamber of a Transwell insert, while GBC cells were placed in the lower chamber. After 5 days of co-culture, T cells and conditioned medium were collected for downstream analysis [30-32]. To investigate the functional role of HIF-1α, we performed experiments as previously described [33]. Briefly, sh-GPX3 cells and their corresponding control cells in the logarithmic growth phase were treated with 20 μM of the HIF-1α-specific inhibitor PX-478 (MCE, HY-10231) or an equivalent volume of DMSO for 24 hours. After treatment, cells were collected for subsequent Western blot (WB) analysis, metabolite quantification, or Seahorse extracellular flux assays to evaluate the impact of HIF-1α inhibition on the relevant phenotypes.

RT-qPCR

Total RNA was extracted from cells using TRIzol (15596026, ThermoFisher, USA), and RNA

concentration and purity were assessed with a NanoDrop 2000 UV–Vis spectrophotometer (ThermoFisher, USA). Complementary DNA (cDNA) was synthesized from mRNA using the PrimeScript RT Reagent Kit (Takara, RR047A, Japan). Gene-specific primers were synthesized by Takara (listed in Supplementary Table 2). Quantitative real-time PCR was carried out on a 7500 Fast Real-Time PCR System (ThermoFisher, 4351106, USA). The relative expression of each target gene was quantified using the $2^{-\Delta\Delta Ct}$ method with GAPDH as the internal reference [34]. Each experiment was repeated three times.

WB

Total proteins from tissues or cells were extracted using RIPA lysis buffer supplemented with PMSF (Beyotime, P0013C). Lysates were incubated on ice for 30 minutes and centrifuged at 8,000 × g for 10 minutes at 4 °C, and the supernatant was collected. Protein concentrations were quantified using the BCA assay (ThermoFisher, 23227, USA). Equal amounts of protein (50 μg) were mixed with 2× SDS loading buffer, boiled for 5 min, separated by SDS–PAGE, and transferred onto PVDF membranes. Membranes were blocked with 5% skim milk for 1 hour at ambient temperature and then incubated overnight at 4 °C with the following primary antibodies: GPX3 (1:1000, Invitrogen, PA5-119141), CD25 (1:200, Abcam, ab231441), CD44 (1:1000, Abcam, ab254530), CD69 (1:1000, Abcam, ab233396), and GAPDH (1:2500, Abcam, ab9485). After three washes with TBST, membranes were incubated for 1 hour with HRP-conjugated goat anti-rabbit IgG (1:2000, Abcam, ab97051). Signal detection was performed using an ECL chemiluminescent kit (Absin, abs920). Images were acquired with the Bio-Rad imaging system (Quantity One v4.6.2), and relative protein expression was calculated as the ratio of target protein intensity to GAPDH intensity [35]. All experiments were repeated in triplicate. Full, un-cropped blot images are provided in Supplementary Figure 5-29.

CCK8 and Flat Plate Cloning Used to Detect Cell Proliferation

Cell proliferation was assessed using the CCK-8 assay (Beyotime, C0037, Shanghai, China). Cancer cells in logarithmic growth were allocated into the indicated groups and adjusted to 5×10^4 cells/mL. A total of 100 μL of cell suspension was seeded into each well of a 96-well plate and incubated for 48 h. After removing the supernatant, 10 μL of CCK-8 reagent was added to each well and incubated at 37 °C for 2 hours. Absorbance at 450 nm was recorded using the Multiskan FC microplate reader (Thermo Fisher, 51119080, USA). Three technical replicates were included per group, and mean values were used for analysis.

For the colony formation assay, cells in exponential growth with viability above 95% were digested, dispersed into single-cell suspensions, and counted. Approximately 100 cells were seeded into 60-mm dishes containing 5 mL of complete medium, gently swirled to ensure uniform distribution, and cultured at 37 °C with 5% CO_2 for 2–3 weeks. Once visible colonies developed, the medium was removed, and the dishes were washed twice with PBS, air-dried, and fixed in methanol for 15 minutes. Fixed cells were stained with Giemsa solution for 10 minutes, rinsed, and air-dried. Colonies containing more than 10 cells were counted under low-magnification microscopy or by visual inspection. The colony formation rate was determined based on the number of colonies relative to the number of seeded cells [36, 37].

Scratch Assay

Cells were cultured for 24 hours before the medium was replaced. A straight scratch was created using a 200-μL pipette tip, and detached cells were removed by washing with PBS. Serum-free medium was added, and images of the scratch area were captured immediately under a microscope. Cultures were then returned to the incubator, and the scratch width was recorded at 0

h and 48 h using ImageJ software [38].

Transwell Assay

Matrigel (Shanghai Haoyang Biotechnology, 356234) was thawed at −80 °C and equilibrated at 4 °C overnight. At 4 °C, 200 μL of serum-free medium was mixed with 200 μL of Matrigel, and 50 μL of the diluted matrix was added to the upper chamber of each Transwell insert. After incubation at 37 °C for 2–3 hours to allow gel polymerization, cells were digested, counted, and resuspended in serum-free medium. A total of 200 μL of cell suspension was added to the upper chamber, while 800 μL of medium containing 20% FBS was added to the lower chamber. After 24 hours of incubation, inserts were washed twice with PBS, and cells remaining on the upper surface were removed with a cotton swab. Cells on the lower surface were fixed with formaldehyde for 10 minutes, washed, and stained with 0.1% crystal violet for 30 minutes. For migration assays, the Transwell inserts were used without Matrigel coating, with all subsequent steps identical to the invasion assay. Cells were imaged and counted under an inverted microscope in at least four randomly selected fields [39]. Experiments were repeated three times.

Detection of Cellular Apoptosis by Flow Cytometry

Apoptosis was quantified using the Annexin V-FITC/PI staining kit (BD Biosciences, 556547). Following staining and flow cytometry acquisition, Annexin V+/PI− cells were classified as early apoptotic, and Annexin V+/PI+ cells as late apoptotic or dead. The sum of these two quadrants represented the total apoptotic fraction [40].

Flow cytometry

Intracellular reactive oxygen species (ROS) levels were assessed using 2',7'-

dichlorofluorescein diacetate (DCFH-DA) (Sigma, D6883, USA). Briefly, 1×10^6 cells were seeded in a 6-well plate, and DCFH-DA was added to each well at a concentration of 10 μM. The cells were incubated at 37°C in a 5% CO_2 incubator for 30 minutes, followed by centrifugation to collect the cells, which were then washed twice and resuspended in PBS. Intracellular ROS levels were measured using a flow cytometer [41].

Live cells were gated based on forward scatter (FS, cell size) and side scatter (SS, granularity). Fluorescence intensity (x-axis) and cell count (y-axis) were used to quantify ROS-positive cells. The percentage of DCF-positive cells represented relative ROS levels. DCFH-DA is oxidized by ROS to form the fluorescent product DCF.

Measurement of ECAR or OCR

Extracellular acidification rate (ECAR) and oxygen consumption rate (OCR) were measured using a Seahorse XF24 Analyzer (Seahorse Biosciences). A total of 1×10^4 cells were seeded into XF96 microplates and allowed to adhere overnight. After equilibration in assay medium for 1 hour at 37 °C, glucose (80 mM), oligomycin (9 μM), and 2-deoxy-D-glucose (2-DG, 1 M) were loaded into ports A, B, and C, respectively. ECAR following glucose addition reflected glycolytic rate, whereas ECAR after oligomycin treatment indicated glycolytic capacity [5]. Basal respiration was defined as the baseline OCR measured before the addition of any inhibitors. ATP production was calculated as the difference in OCR before and after the addition of oligomycin (an ATP synthase inhibitor), reflecting the amount of OCR attributable to mitochondrial ATP synthesis. Maximal respiration was determined from the peak OCR induced by FCCP (an uncoupling agent), representing the maximum mitochondrial respiratory capacity. Spare respiratory capacity was calculated as the difference between maximal and basal respiration, indicating the ability of mitochondria to meet increased energetic demand. Non-mitochondrial respiration was defined by

the remaining OCR after antimycin A and rotenone treatment (complex III and complex I inhibitors), reflecting oxygen consumption from non-mitochondrial sources. The metabolic phenotypes were determined by the relative levels of ECAR (reflecting glycolysis) and OCR (reflecting oxidative phosphorylation): high ECAR/low OCR indicates a glycolytic phenotype; low ECAR/high OCR indicates an oxidative phenotype; high ECAR/high OCR indicates a highly energetic phenotype; and low ECAR/low OCR indicates a quiescent phenotype [42].

ELISA and Metabolite Detection

Supernatants from T cell–GBC co-culture systems and mouse blood were collected and centrifuged to remove debris. Concentrations of IL-2, IFN-γ, and TNF-α were quantified using ELISA kits, including Human IL-2 (SEKH-0008), Mouse IL-2 (SEKM-0004), Human IFN-γ (SEKH-0046), Mouse IFN-γ (SEKH-0031), Human TNF-α (SEKH-0047), and Mouse TNF-α (SEKH-0034) kits (Solarbio).

For metabolite analysis, cells were washed with PBS and lysed, followed by centrifugation to obtain clarified lysates. Malondialdehyde (MDA), L-lactate, and pyruvate levels in cell lysates and mouse serum were measured using the MDA Content Detection Kit (BC0025), L-Lactate Content Detection Kit (BC2235), and Pyruvate Content Detection Kit (BC2205) from Solarbio [43, 44].

***In vivo* Mouse Experiments**

A total of 32 male NODs.Cg-Prkdc^{scid} Il2rg^{tm1Wjl}/SzJ (NSG) mice aged 5-6 weeks were obtained from The Jackson Laboratory and kept in SPF-level animal facilities. Animals were housed individually at 22–25 °C with 60–65% humidity. After one week of acclimatization, all mice underwent health evaluation before experimentation. The experimental procedures and animal use protocols were approved by the Institutional Animal Ethics Committee of Peking Union

Medical College Hospital, Chinese Academy of Medical Science and Peking Union Medical College (No. I-23PJ352).

To establish the subcutaneous graft transplantation model of GBC, the mice were randomly assigned to four groups (oe-NC, oe-GPX3, sh-NC, sh-GPX3; n = 5 per group). Cell suspensions of GBC-SD cells overexpressing GPX3 or NOZ cells with GPX3 knockdown (2×10^7 cells/mL; 0.2 mL per mouse) were prepared following lentiviral transduction and injected subcutaneously into the left axilla. Tumor volumes were measured every 5 days beginning on day 7. On day 27, mice were anesthetized with isoflurane (Chemical Book, 26675-46-7) and injected intraperitoneally with D-luciferin (150 mg/kg; Merck, 2591-17-5). After 10 minutes, white-light and bioluminescent images were acquired using the IVIS Lumina XR system (PerkinElmer). Mice were euthanized on day 30, and tumors were excised and measured. Tumor volume was calculated as: $V = L \times W^2 \times 1/2$ (V represents volume, L represents length, and W represents width).

To investigate whether GPX3 affects tumor metastasis in mice, another group of mice was kept, and 2×10^6 cells were injected into their spleens. The injected groups corresponded to the subcutaneous injection model groups (oe-NC, oe-GPX3, sh-NC, and sh-GPX3), with 5 mice in each group. After 1 month from injection, the mice were euthanized, and their livers were collected to count the number of metastatic nodules in each group [45, 46].

For *in vivo* pharmacologic validation, we first established a xenograft model by subcutaneously injecting NOZ cells stably expressing sh-NC or sh-GPX3 into NSG mice. Once tumors reached approximately 100 mm^3, mice were randomly allocated to four treatment groups: sh-NC + Vehicle, sh-NC + PX-478, sh-GPX3 + Vehicle, and sh-GPX3 + PX-478. Mice received PX-478 (20 mg/kg) or vehicle by oral gavage once daily for 5 consecutive days [47]. Tumor size and body weight were monitored throughout treatment. At study completion, *in vivo* imaging was performed using IVIS prior to euthanasia. Tumor tissues and serum samples were collected for

immunohistochemistry, WB, and ELISA to assess the impact of HIF-1α inhibition on tumor growth, metabolic characteristics, and the immune microenvironment.

H&E Staining

Paraffin-embedded mouse tissue sections were deparaffinized and rehydrated before staining. Hematoxylin and eosin (H&E) staining was carried out following the instructions of the H&E Staining Kit (Shanghai Bogu Biological Technology, PT001). Briefly, sections were stained with hematoxylin for 10 minutes at ambient temperature, rinsed in running water for 30–60 seconds, differentiated in 1% hydrochloric acid alcohol for 30 s, and washed for 5 min. Slides were then stained with eosin for 1 min and dehydrated through a graded ethanol series (70%, 80%, 90%, 95%, and 100%; 1 min each). After clearing in xylene for 1 minute and repeating the clearing step twice in xylene I and II, sections were mounted with neutral resin. Tissue morphology was examined and imaged using an Olympus BX50 optical microscope (Olympus, Tokyo) [48].

Immunohistochemistry (IHC)

Formalin-fixed tissues were dehydrated through graded ethanol and embedded in paraffin. Paraffin blocks were sectioned at 5 μm and baked at 60 °C for 20 minutes. Sections were then deparaffinized in xylene twice (15 min each) and rehydrated through absolute ethanol (two changes, 5 min each), followed by 95% and 70% ethanol (10 min each). Endogenous peroxidase activity was quenched using 3% H_2O_2 for 10 min at ambient temperature. For antigen retrieval, sections were heated in citrate buffer using microwave treatment for 3 minutes and then incubated in retrieval buffer for 10 minutes, followed by three PBS washes. Slides were blocked with normal goat serum (Shanghai Haoran Biotechnology, C-0005) for 20 minutes and incubated overnight at 4 °C with primary antibodies: anti-HK2 (1:500, Abcam, ab209847), anti-Ki67 (1:200, Abcam,

ab15580), and anti-8-OHdG (1:200, Abcam, ab48508). The next day, sections were incubated with goat anti-rabbit IgG secondary antibody (1:1000, Abcam, ab6721) for 30 minutes, followed by SABC reagent (SinoBiological, SA0041) at 37 °C for 30 minutes. Visualization was performed using the DAB chromogenic kit (SinoBiological, DA1010) for 6 min, and slides were counterstained with hematoxylin (Beyotime, C0107) for 30 s. After dehydration through 70%, 80%, 90%, 95%, and absolute ethanol (2 min each), sections were cleared twice in xylene (5 min each) and mounted with neutral resin. Images were acquired using an Olympus BX63 microscope. PBS substituted for primary antibody served as the negative control. Five randomly selected fields were analyzed per section. Brown-stained cells were counted as positive cells, and the percentage of positive cells was calculated based on the proportion of positive cells relative to the total number of cells in each field [49]. All experiments were performed in triplicate.

Measurement of the GSH/GSSG ratio

The reduced and oxidized glutathione ratio was quantified using a commercial enzymatic cycling assay kit (Beyotime, S0053). Briefly, samples were differentially pretreated to measure GSH and GSSG separately: total glutathione was measured directly from tissue homogenates or cell lysates, whereas GSSG was measured after incubating a separate aliquot with a GSH-scavenging reagent to remove reduced GSH. The reaction system contained glutathione reductase, NADPH, and the chromogenic reagent DTNB. Absorbance at 412 nm was monitored kinetically using a microplate reader. Standard curves were used to calculate the absolute concentrations of GSH and GSSG, and their ratio was used as an indicator of the cellular redox state. All samples were measured in triplicate, and experiments were repeated independently three times. Results were normalized to total protein content [50].

Statistical Analysis

All statistical analyses were carried out using GraphPad Prism 9 (GraphPad Software, USA). Data are expressed as mean ± standard deviation. Prior to hypothesis testing, datasets were examined for normal distribution and equal variance. Differences between two groups were evaluated using unpaired t-tests when these assumptions were satisfied. For comparisons across multiple groups, either one-way ANOVA or repeated-measures ANOVA was performed as appropriate. A *P v*alue < 0.05 was regarded as statistically significant.

Results

Identification of Key Genes and Pathways in GBC

To identify biomarkers associated with GBC progression, high-quality total RNA was isolated from tissues of three GBC patients and three healthy controls and subjected to high-throughput RNA sequencing (RNA-seq). Differential expression analysis revealed 2,918 DEGs, comprising 1,405 upregulated and 1,513 downregulated genes (Figure 1A–B). Principal component analysis (PCA) was then performed to assess global transcriptional differences. As shown in Figure 1C, cancer and normal samples separated clearly along both PC1 and PC2, demonstrating distinct transcriptomic profiles between the two groups.

We further analyzed the GBC-related transcriptomic dataset GSE139682 from the GEO database, which contains 10 GBC and 10 normal tissue samples. After clustering all samples and determining the optimal soft-thresholding power (Figure 1D; Supplementary Figure 1A), a WGCNA was constructed. Gene clustering yielded 25 co-expression modules (Supplementary Figure 1B), and their correlations with GBC were visualized in a module–trait heatmap. The module showing the strongest association with GBC (r = 0.76, *P* < 0.01) contained 559 genes and

was selected for downstream analysis (Supplementary Figure 1C-E).

To identify robust GBC-related genes, these WGCNA-derived hub genes were intersected with the DEGs from our RNA-seq dataset, resulting in 126 overlapping key genes (Figure 1E). Functional enrichment analysis revealed that these genes were primarily associated with biological processes such as muscle cell and striated muscle cell differentiation, and muscle contraction. They were enriched in cellular components, including contractile fibers, myofibrils, and stress fibers, and showed molecular functions such as actin binding, heparin binding, and glycosaminoglycan binding. KEGG pathway analysis indicated potential involvement in the cGMP–PKG signaling pathway, PI3K–Akt signaling pathway, and ECM–receptor interaction (Figure 1F).

In summary, transcriptomic profiling combined with WGCNA identified 126 key genes potentially contributing to GBC pathogenesis.

Differential Protein Expression Analysis Reveals GPX3 as a Key Gene in GBC Progression

To identify protein-level alterations associated with GBC progression, proteomic sequencing was performed on normal gallbladder tissues (Normal group), preneoplastic lesions (Preneoplastic group), and GBC tissues (Tumor group), with six samples per group. Differential expression analysis showed no detectable DEPs between the Preneoplastic and Normal groups (Supplementary Figure 2A). The Tumor group had 83 DEPs compared to the Preneoplastic group, with 75 proteins significantly up-regulated and 8 proteins significantly down-regulated (Supplementary Figure 2B). The Tumor group had 689 DEPs compared to the Normal group, with 609 proteins significantly up-regulated and 80 proteins significantly down-regulated (Figure 2A).

PCA was conducted to compare the global proteomic profiles across the three groups. As shown in Supplementary Figure 2C, the Normal and Preneoplastic samples largely overlapped, indicating minimal proteomic variation between them. In contrast, the Tumor samples were clearly

separated from both comparison groups along the PC1 and PC2 axes, with the most pronounced divergence observed between the Tumor and Normal groups (Supplementary Figure 2D; Figure 2B). These findings reveal substantial proteomic differences associated with tumor progression. Based on these results, we selected the Tumor and Normal groups with the most significant differences and generated a heat map of the top 50 significantly up-regulated and down-regulated proteins (Figure 2C).

Further analysis was conducted on the DEPs between the Tumor and Normal groups using GO and KEGG enrichment analysis (Figure 2D-E). GO analysis indicated that these proteins were mainly enriched in biological processes such as ribonucleoprotein complex biogenesis, ribosome biogenesis, and ncRNA processing. They were localized predominantly in mitochondrial and organellar ribosomes as well as spliceosomal complexes, and exhibited molecular functions including catalytic activity on RNA, snoRNA binding, and ATP hydrolysis. KEGG analysis revealed enrichment in pathways such as Spliceosome, Ribosome biogenesis in eukaryotes, and Nucleocytoplasmic transport.

To identify the most robust GBC-associated gene, we integrated four datasets, including RNA-seq-derived DEGs, WGCNA-identified hub genes, proteomics-derived DEPs, and GBC-related genes from the GeneCards database. This intersection yielded a single candidate gene, GPX3 (Figure 2F). GPX3 is a glutathione peroxidase enzyme and is considered a tumor suppressor [51]. It has been reported that GPX3 can inhibit cancer-cell proliferation, migration, and invasion through oxidative stress–related mechanisms [20]. Consistent with these reports, both RNA-seq and proteomic data demonstrated marked downregulation of GPX3 in GBC tissues compared with Normal samples (Supplementary Figure 2E–F). Because TCGA lacks GBC datasets, we analyzed cholangiocarcinoma (CHOL) transcriptomes, which represent a closely related biliary tract malignancy. GPX3 was similarly reduced in CHOL tumor tissues (Supplementary Figure 2G).

These findings were further validated by RT-qPCR and WB, which confirmed a significant decrease in GPX3 mRNA and protein levels in GBC tumors (Figure 2G-H).

Collectively, these results identify GPX3 as a key downregulated gene and suggest its potential involvement in the regulation of GBC progression.

Metabolomics Reveals GPX3 Involvement in GBC through Oxidative Stress and the Warburg Effect

Metabolomics, an analytical approach enabling high-throughput profiling of small-molecule metabolites, has become an important tool for uncovering metabolic alterations in human diseases. The rapid growth in this field has sparked renewed interest in understanding the role of metabolism and small molecule metabolites in various biological processes [52]. In recent years, metabolomics, together with transcriptomic profiling, has increasingly been applied to identify critical molecular alterations driving tumor development [53, 54]. To further explore the potential mechanisms of GPX3 in regulating the occurrence and progression of GBC, LC-MS/MS was utilized to analyze metabolites in 6 cases of GBC and 6 cases of adjacent normal tissues. The metabolomic data were normalized using the MetaboAnalyst 5.0 database (Supplementary Figure 3A) and subjected to PCA analysis for dimension reduction, revealing some overlap between Normal and Tumor samples along the PC1 and PC2 axes (Supplementary Figure 3B). A total of 122 differentially expressed metabolites were identified using a |Fold change| > 2 cutoff, with 48 upregulated and 74 downregulated metabolites (Supplementary Figure 3C). Subsequently, a T-test was performed, and 59 differentially expressed metabolites were identified using a p-value cutoff of less than 0.05 (Supplementary Figure 3D). By combining the results from the Fold change and T-test analyses and plotting them on a volcano plot, 50 differentially expressed metabolites were identified, including 15 upregulated and 35 downregulated metabolites (Figure 3A). Heatmaps were

generated to visualize the relative abundance of metabolites among different groups (Figure 3B).

To further evaluate the changes in metabolites, an OPLS-DA model was constructed, and score plots were generated for each group, clearly separating the Tumor group from the Normal group (Supplementary Figure 3E). Based on the OPLS-DA results, 138 metabolites were selected based on the criteria of having a VIP ＞1, as indicated by the S-plot and VIP plot (Supplementary Figure 3F, Figure 3C).

By integrating the differentially expressed metabolites selected through log2FC, T-test, and OPLS-DA methods, a Venn diagram was used to identify 50 common differentially expressed metabolites (Figure 3D). KEGG enrichment analysis showed that these metabolites were predominantly associated with pathways such as alanine, aspartate and glutamate metabolism, arginine biosynthesis, and nicotinate and nicotinamide metabolism. Analysis based on the SMPDB database further revealed enrichment in pathways linked to the Warburg effect, methionine metabolism, and the mitochondrial electron transport chain (Figure 3E-F).

Notably, the KEGG and SMPDB enrichment analysis indicated the involvement of glutamate metabolism and the Warburg effect in the differentially expressed metabolites. As GPX3 is an antioxidant enzyme that uses glutathione (GSH) as a substrate to reduce peroxides and helps resist oxidative stress, glutamate is one of the key precursors for GSH synthesis [55]. It has been reported that excessive oxidative stress leads to the metabolic shift of cancer cells towards aerobic glycolysis, enhancing the Warburg effect [56].

Based on the results of the bioinformatics analysis, the data from transcriptomics, proteomics, and metabolomics were analyzed together (Figure 4). Our hypothesis is that GPX3 may regulate the occurrence and progression of GBC by altering the oxidative stress status of cells and participating in the Warburg effect.

GPX3 Modulation Impacts Vitality, Proliferation, Migration, and Invasion in GBC Cells

To assess the relevance of GPX3 in GBC progression, we quantified GPX3 expression in five human GBC cell lines (EH-GB1, NOZ, GBC-SD, OCUG-1, and SGC-996) and in human gallbladder epithelial cells (HGBEC) using RT-qPCR and WB. GPX3 mRNA and protein levels were markedly reduced in all GBC cell lines compared with HGBEC. Among them, NOZ cells displayed relatively higher GPX3 expression, whereas GBC-SD cells exhibited the lowest levels (Supplementary Figure 4A). Based on these findings, we selected the NOZ and GBC-SD cell lines for subsequent studies.

Using lentivirus, we silenced GPX3 in NOZ cells and overexpressed GPX3 in GBC-SD cells, successfully establishing stable cell lines. RT-qPCR results confirmed effective GPX3 overexpression and silencing, with sh-GPX3-1 exhibiting the strongest knockdown efficiency (Supplementary Figure 4B). Consequently, sh-GPX3-1 was chosen for further experiments. WB analysis further confirmed that GPX3 protein expression was significantly upregulated in oe-GPX3 GBC-SD cells and downregulated in sh-GPX3 NOZ cells. Additionally, GPX3-MUT overexpression in sh-GPX3 NOZ cells significantly increased GPX3 protein expression compared to the MUT-CON group (Supplementary Figures 4C-D).

Using the GPX3-overexpressing GBC-SD and GPX3-silenced NOZ cell lines established via lentiviral infection, we conducted a series of functional assays (Figure 5A). CCK-8 and colony formation analyses showed that forced GPX3 expression markedly reduced cell viability and proliferative capacity in GBC-SD cells, whereas GPX3 knockdown significantly enhanced both parameters in NOZ cells. Importantly, introducing the GPX3-MUT construct into sh-GPX3 NOZ cells effectively reversed the increase in viability and proliferation caused by GPX3 loss (Figures 5B-C).

Cell migration, assessed using Transwell and scratch assays, revealed that GPX3

overexpression markedly reduced migration in GBC-SD cells, whereas GPX3 silencing enhanced migration in NOZ cells. GPX3-MUT overexpression in sh-GPX3 NOZ cells significantly reduced their migration ability (Figures 5D-E). Similarly, cell invasion analysis via Transwell assays demonstrated that GPX3 overexpression significantly inhibited invasion in GBC-SD cells, while GPX3 silencing increased invasion in NOZ cells. GPX3-MUT overexpression in sh-GPX3 NOZ cells significantly suppressed invasion (Figure 5F).

Flow cytometry analysis of apoptosis revealed that GPX3 overexpression significantly increased apoptosis in GBC-SD cells, while GPX3 silencing reduced apoptosis in NOZ cells. GPX3-MUT overexpression in sh-GPX3 NOZ cells significantly enhanced apoptosis levels (Figure 5G).

In summary, these results demonstrate that GPX3 upregulation markedly suppresses GBC cell viability, proliferation, migration, and invasion, while simultaneously enhancing apoptotic activity.

GPX3 Modulation Alters Metabolic Reprogramming and Immune Activation in GBC Cells

In the metabolomics analysis, we examined the differential metabolites and found enrichment of metabolites involved in the Warburg effect. The Warburg effect, a hallmark of cancer, is characterized by enhanced glycolysis and suppressed oxidative phosphorylation in the presence of oxygen [57].

We first measured ROS levels in cells using flow cytometry. The results showed that GPX3 overexpression significantly reduced ROS levels in GBC-SD cells, whereas GPX3 silencing significantly increased ROS levels in NOZ cells. In sh-GPX3 NOZ cells, GPX3-MUT overexpression significantly reduced ROS levels (Figure 6A). Measurement of the GSH/GSSG ratio revealed a marked increase in the oe-GPX3 group relative to the control, whereas GPX3 knockdown produced the opposite effect. Notably, re-expression of GPX3 via the GPX3-MUT

construct in sh-GPX3 NOZ cells significantly restored the GSH/GSSG ratio (Figure 6B). Consistently, MDA levels, an indicator of oxidative stress, were assessed using an assay kit. GPX3 overexpression substantially reduced MDA levels, while GPX3 silencing led to a pronounced increase. GPX3-MUT overexpression similarly lowered MDA accumulation in sh-GPX3 NOZ cells (Figure 6C).

Analysis of ECAR revealed that GPX3 overexpression inhibited ECAR in GBC-SD cells, while GPX3 silencing enhanced ECAR in NOZ cells. In sh-GPX3 NOZ cells, GPX3-MUT overexpression inhibited ECAR (Figure 6D). Similarly, OCR measurements, reflecting mitochondrial respiratory activity, demonstrated that GPX3 overexpression enhanced OCR, whereas GPX3 knockdown markedly reduced it. Restoration of GPX3 expression through GPX3-MUT significantly increased OCR in sh-GPX3 NOZ cells (Figure 6E). In addition, we calculated basal respiration, maximal respiration, ATP production, spare respiratory capacity, and non-mitochondrial respiration based on the OCR and ECAR data (Figure 6F) and presented the corresponding metabolic phenotypes (Figure 6G). The results showed that GPX3 overexpression markedly increased basal and maximal respiration, ATP-linked respiration and spare respiratory capacity compared with the corresponding controls, whereas GPX3 knockdown significantly reduced these parameters. Re-expression of the catalytic mutant GPX3-MUT in sh-GPX3 cells failed to rescue the impaired mitochondrial respiration. Consistently, metabolic phenotyping revealed that oe-GPX3 cells shifted toward an oxidative, highly energetic phenotype, while sh-GPX3 and GPX3-MUT cells clustered in the low-energy/glycolytic region (Figure 6F-G). Additionally, lactate and pyruvate levels, the end products of glycolysis, were assessed using assay kits. GPX3 overexpression significantly reduced lactate and pyruvate levels compared to the control group, while GPX3 silencing significantly increased their levels. In sh-GPX3 NOZ cells, GPX3-MUT overexpression significantly reduced lactate and pyruvate levels (Figure 6H). These

results suggest that GPX3 overexpression inhibits glycolysis in GBC cells.

Immune evasion and metabolic reprogramming are two fundamental hallmarks of cancer [58]. Enhanced aerobic glycolysis in tumor cells not only promotes cancer cell growth and metastasis but also facilitates tumor immune evasion [59, 60]. To evaluate whether GPX3 influences tumor–immune interactions, GBC cells and T cells were co-cultured using Transwell chambers (Figure 6I). WB analysis showed that T cells cultured with oe-GPX3 GBC-SD cells exhibited markedly increased expression of the activation markers CD25, CD44, and CD69 compared with controls. In contrast, T cells co-cultured with sh-GPX3 NOZ cells displayed reduced levels of these activation markers. Importantly, reintroduction of GPX3 via the GPX3-MUT construct in sh-GPX3 NOZ cells restored CD25, CD44, and CD69 expression in co-cultured T cells (Figure 6J).

ELISA was performed to quantify IL-2, IFN-γ, and TNF-α levels in the T-cell culture supernatant. T cells co-cultured with oe-GPX3 GBC-SD cells produced significantly higher levels of all three cytokines compared with controls, whereas cytokine production was markedly reduced in the sh-GPX3 NOZ group. Notably, re-expression of GPX3 through the GPX3-MUT construct in sh-GPX3 NOZ cells restored IL-2, IFN-γ, and TNF-α secretion (Figure 6K).

In summary, our results demonstrate that GPX3 overexpression reduces oxidative stress and glycolysis in GBC cell lines while enhancing T-cell activation and cytokine secretion.

GPX3 Integrates Metabolic Reprogramming and Immune Evasion through the HIF-1α Signaling Pathway

To elucidate the molecular mechanism through which GPX3 regulates glycolysis and immune escape, we performed an in-depth analysis of downstream signaling pathways. Previous studies have shown that ROS can stabilize HIF-1α, a key transcriptional activator of the Warburg effect, and can also directly suppress T-cell activation and function [61, 62]. Based on these findings, we

hypothesized that the ROS accumulated after GPX3 loss may activate the HIF-1α signaling pathway, thereby coordinately driving metabolic reprogramming and immune suppression. First, we measured HIF-1α protein levels in GBC cells. WB results showed that HIF-1α expression was markedly reduced in GPX3-overexpressing GBC-SD cells but significantly increased in GPX3-silenced NOZ cells (Figure 7A), consistent with GPX3-mediated regulation of intracellular ROS.

To determine whether HIF-1α acts as a key downstream effector of GPX3 function, we treated GPX3-silenced NOZ cells with the HIF-1α inhibitor PX-478 (25 μM). Inhibition of HIF-1α partially reversed GPX3-loss–induced glycolytic enhancement, as indicated by reduced lactate and pyruvate levels (Figure 7B) and decreased ECAR (Figure 7C). More importantly, in the co-culture experiments (Figure 7D), HIF-1α inhibition partially restored T-cell activation, reflected by increased expression of activation markers (CD25, CD44, CD69) (Figure 7E) and elevated levels of IFN-γ, IL-2, and TNF-α in the culture supernatant (Figure 7F).

These findings indicate that HIF-1α serves as a critical downstream node of GPX3. GPX3 loss leads to ROS accumulation, which stabilizes and activates HIF-1α. Activated HIF-1α enhances glycolysis while suppressing T-cell immune function, thereby jointly promoting gallbladder cancer progression through coordinated metabolic and immune remodeling.

Enhanced Tumor Growth and Immune Evasion in GPX3-silenced GBC Cells

To verify these results, we selected 20 humanized NSG mice and established a xenograft model of GBC by subcutaneously injecting GBC-SD cells overexpressing GPX3 or NOZ cells with silenced GPX3 into the axilla with lentivirus. Tumor growth was then assessed (Figure 8A). Tumor growth analysis showed that GPX3 overexpression markedly slowed tumor progression, whereas GPX3 silencing significantly accelerated tumor growth (Figure 8B). Through *in vivo* IVIS imaging to detect the size of orthotopically transplanted tumors followed by euthanizing and

sampling of the mice, the results revealed that overexpression of GPX3 significantly inhibited tumor volume and weight, whereas silencing of GPX3 markedly increased tumor volume and weight (Figure 8C-D).

Next, histological staining of tumor tissues was performed. H&E staining showed that oe-GPX3 increased cellular density and improved structural integrity, while sh-GPX3 reduced cell density and caused structural disruption (Figure 9A). Additionally, IHC analysis and biochemical assays showed that tumors from the oe-GPX3 group displayed markedly lower oxidative stress and reduced serum MDA levels, whereas the sh-GPX3 group demonstrated the opposite pattern (Figure 9B-C).

ELISA results showed that serum IL-2, IFN-γ, and TNF-α levels were markedly elevated in the oe-GPX3 group, whereas all three cytokines were significantly reduced in the sh-GPX3 group (Figure 9D). Consistently, WB analysis of tumor tissues revealed that GPX3 overexpression enhanced the expression of the T-cell activation markers CD25, CD44, and CD69, while GPX3 silencing led to their pronounced downregulation (Figure 9E), indicating that loss of GPX3 may facilitate immune escape in GBC.

To further evaluate metastatic potential, lentivirus-infected GBC-SD or NOZ cells were injected into the spleens of another cohort of mice using the same grouping strategy (oe-NC, oe-GPX3, sh-NC, sh-GPX3; n = 3/group). One month later, liver tissues were collected for H&E staining. Mice injected with GPX3-overexpressing cells exhibited fewer liver metastatic nodules, whereas GPX3-silenced cells markedly increased metastatic burden (Figure 9F).

These results indicate that silencing of GPX3 promotes the occurrence and progression of GBC, increases oxidative stress and glycolysis, and further facilitates immune evasion and metastasis in GBC.

In Vivo Inhibition of HIF-1α Reverses GPX3-Silencing–Induced Tumor Growth and Immune Suppression

To validate that HIF-1α acts as a key downstream effector of GPX3 *in vivo*, we performed pharmacological intervention experiments in a mouse xenograft model. NOZ cells stably expressing sh-GPX3 or their corresponding controls were subcutaneously injected into NSG mice. When tumors reached approximately 100 mm^3, mice were randomized into four groups (sh-NC + vehicle, sh-GPX3 + vehicle, sh-NC + PX-478, sh-GPX3 + PX-478) and treated orally with the HIF-1α inhibitor PX-478 (20 mg/kg) or vehicle for five consecutive days (Figure 10A).

The results showed that in mice injected with sh-GPX3 NOZ cells, PX-478 treatment markedly inhibited tumor progression, reflected by significantly reduced tumor volume and final tumor mass compared with vehicle-treated controls (Figure 10B, C). IVIS imaging further demonstrated a pronounced decrease in bioluminescent intensity in PX-478–treated tumors (Figure 10D).

Histological examination of tumor tissues showed that sh-GPX3 reduced cellular density and impaired tissue structure, whereas PX-478 effectively reversed these changes. IHC analysis revealed that tumor tissues in the sh-GPX3 group expressed markedly higher levels of the glycolytic enzyme HK2 and the proliferation marker Ki-67 than controls, and PX-478 treatment effectively reversed this elevated expression (Figure 10E). This indicates that in vivo inhibition of HIF-1α can antagonize the enhanced glycolysis and cell proliferation driven by GPX3 loss.

Importantly, we also assessed the immune status of the tumor microenvironment. WB analysis of tumor lysates confirmed that PX-478 treatment enhanced the expression of T-cell activation markers CD25 and CD69 (Figure 10F). ELISA analysis of mouse serum further showed that PX-478 significantly increased circulating IFN-γ and TNF-α levels in the sh-GPX3 group (Figure 10G).

Collectively, these *in vivo* results provide strong evidence that HIF-1α is a critical downstream

mediator of GPX3's tumor-suppressive function. Pharmacologic inhibition of HIF-1α significantly reverses the malignant tumor growth and immunosuppressive microenvironment induced by GPX3 loss.

Discussion

Previous studies have established that GPX3 is downregulated in GBC and is associated with oxidative stress [63-65]. However, its systematic regulatory role in shaping the tumor metabolic and immune microenvironment has remained unclear. By integrating multi-omics profiling with *in vitro* and *in vivo* functional assays, our study not only confirms the association between GPX3 downregulation, oxidative stress, and enhanced glycolysis but also uncovers its integrative role in promoting immune evasion and metastasis through the reprogramming of cellular energy metabolism.

Our data show that GPX3 loss leads to ROS accumulation, increased levels of key glycolytic intermediates, impaired mitochondrial function, and a decreased GSH/GSSG ratio. These phenomena indicate profound metabolic remodeling [66, 67]. We propose that ROS act as critical signaling mediators through which the antioxidant enzyme GPX3 regulates glycolysis. Our findings suggest that accumulated ROS can stabilize the master metabolic transcription factor HIF-1α, thereby increasing the expression of multiple glycolytic enzymes. In addition, previous studies have shown that ROS can directly oxidize key glycolytic enzymes such as GAPDH and PKM2, altering their enzymatic activity and rewiring metabolic flux [68, 69]. To counteract oxidative stress arising from GPX3 deficiency, tumor cells may also activate the pentose phosphate pathway (PPP), generating additional NADPH to maintain reduced GSH and support GSH regeneration. Enhanced PPP activity may divert glucose flux while coexisting with elevated glycolysis, collectively supporting biosynthetic and antioxidant demands [70]. Notably, such metabolic

remodeling may extend beyond glycolysis to include the activation of alternative biosynthetic pathways such as lipogenesis (e.g., via ACLY).

The antitumor characteristics of GPX3 are largely linked to redox-dependent signaling. Prior studies demonstrated that GPX3 overexpression inhibits proliferation, migration, and invasion in lung cancer cells by suppressing ROS-mediated NF-κB activation [20]. Building on this foundation, our work directly links GPX3 function to the HIF-1α signaling axis. In GBC, we demonstrate that GPX3 loss leads to ROS accumulation and stabilization of HIF-1α protein, whereas pharmacologic inhibition of HIF-1α effectively reverses the glycolytic, proliferative, and immunosuppressive phenotypes induced by GPX3 deficiency. These findings suggest that the GPX3–ROS–HIF-1α axis represents a central regulatory mechanism in GBC. Our transcriptomic analyses also reveal that GPX3-associated differentially expressed genes are enriched in pathways such as PI3K–Akt, which share extensive crosstalk with HIF-1α regulation. The functional relevance of these interactions warrants further investigation.

A key finding of this study is the link between GPX3-regulated metabolic reprogramming and the tumor immune microenvironment. GPX3 depletion–driven glycolytic activation was closely associated with impaired T-cell function, likely due to intensified competition for glucose between glycolytic tumor cells and infiltrating T cells, as well as the buildup of lactate and other immunosuppressive metabolites that collectively dampen antitumor immunity. Our *in vivo* findings further demonstrate that GPX3-low tumors display increased growth and metastatic potential, accompanied by reduced expression of T-cell activation markers; importantly, inhibition of HIF-1α restores antitumor immune activity, confirming the functional relevance of this metabolic-immune axis.

From a translational perspective, our study provides preliminary evidence linking GPX3 expression levels to malignant progression in GBC. Although our retrospective analysis shows that

low GPX3 expression correlates with adverse pathological features, we acknowledge the need for prospective clinical cohorts and deeper mining of public datasets (e.g., TCGA, GEO) to robustly establish the prognostic value of GPX3. More importantly, our mechanistic findings highlight a novel therapeutic angle for targeting GPX3-low tumors. GPX3-deficient tumors exhibit increased sensitivity to the HIF-1α inhibitor PX-478, suggesting that targeting the downstream HIF-1α pathway may represent a promising precision therapy strategy. Future therapeutic development should not be restricted to restoring GPX3 itself but should focus on vulnerable downstream nodes such as HIF-1α and its associated metabolic–immune crosstalk network.

Despite these advances, several limitations should be acknowledged. First, the sample size is relatively small, and validation in larger, independent cohorts will be essential to strengthen the reliability of our conclusions. Second, although we reveal metabolic remodeling induced by GPX3 loss, the underlying molecular network remains incompletely characterized. The direct causal relationship between ROS accumulation and HIF-1α stabilization requires more precise genetic validation. Moreover, the direct oxidative modifications of key glycolytic enzymes such as GAPDH and PKM2 by ROS and their functional consequences remain to be demonstrated through site-specific mutagenesis and related approaches. Additionally, the dynamic interplay among glycolysis, the PPP, and other alternative pathways such as lipogenesis has not yet been fully elucidated. Finally, how such broad metabolic rewiring globally coordinates cell fate decisions—including survival, proliferation, or apoptosis—remains an important question for future research. The specific regulatory circuitry linking GPX3 to its downstream pathways also requires further clarification.

Overall, our study identifies GPX3 as a critical molecular link between oxidative stress, metabolic reprogramming, and immune evasion in GBC. More importantly, we propose a new therapeutic strategy centered on targeting downstream effectors of GPX3, particularly HIF-1α.

These findings provide a strong mechanistic rationale and a promising intervention framework for overcoming current therapeutic challenges in GBC (**Figure 11**).

Ethics Approval and Consent to Participate

This study was approved by the Ethics Committee of Peking Union Medical College Hospital, Chinese Academy of Medical Science and Peking Union Medical College (Approval No. I-23PJ352). All procedures were performed in accordance with the principles of the Declaration of Helsinki. Written informed consent was obtained from all individual participants included in the study.

The experimental procedures and animal use protocols were approved by the Institutional Animal Ethics Committee of Peking Union Medical College Hospital, Chinese Academy of Medical Science and Peking Union Medical College (No. I-23PJ352).

Acknowledgment

Not applicable.

Funding

This study was supported by the Postdoctoral Fellowship Program of China Postdoctoral Science Foundation (GZC20251430), Beijing Bethune Charitable Foundation (GDZL040), Chinese Academy of Medical Sciences Innovation Fund for Medical Sciences (No.2022-I2M-C&T-A-004), National High Level Hospital Clinical Research Funding (No.2022-PUMCH-B-005), Fundamental Research Funds for the Central Universities (3332024119), Scientific Research Promotion Program for Clinical Medicine (2025CMFA08), Basic and Applied Basic Research Foundation of Guangdong Province (2023A1515220211), and Guangzhou Municipal Science and Technology Project (2024B03J1335).

Conflict of Interest

The author declares no conflict of interest.

Data Availability

The proteomics data have been deposited in public databases. The data can be accessed through the following identifiers:

iProX: ID IPX0011270000

ProteomeXchange: ID PXD061486

The sequencing data have been uploaded to the NCBI database under the following identifiers:

Submissions: SUB15151673

BioProject: PRJNA1231233

SRA IDs:

Paracancerous group: SRR32560247, SRR32560246, SRR32560245

Tumor group: SRR32560244, SRR32560243, SRR32560242

All data are publicly available and can be accessed via the provided links.

Author Contributions

Zuyi Ma: Conceptualization, Investigation, Formal Analysis, Writing – Original Draft.

Jia Sun: Investigation, Validation, Data Curation.

Xin Wu: Investigation, Methodology.

Changzhen Shang: Supervision, Resources, Writing – Review & Editing, Funding Acquisition.

Binglu Li: Supervision, Project Administration, Writing – Review & Editing, Funding Acquisition.

All authors reviewed and approved the final manuscript.

Consent for publication

Not applicable.

References

1 Pearson-Stuttard J, Papadimitriou N, Markozannes G, Cividini S, Kakourou A, Gill D *et al.* Type 2 Diabetes and Cancer: An Umbrella Review of Observational and Mendelian Randomization Studies. Cancer Epidemiology, Biomarkers & Prevention. 2021; **30**: 1218–1228.

2 Huang J, Lucero-Prisno DE III, Zhang L, Xu W, Wong SH, Ng SC *et al.* Updated epidemiology of gastrointestinal cancers in East Asia. Nat Rev Gastroenterol Hepatol. 2023; **20**: 271–287.

3 Brooks GA. Lactate as a fulcrum of metabolism. Redox Biology. 2020; **35**: 101454.

4 Singh N, Kazim SN, Sultana R, Tiwari D, Borkotoky R, Kakati S *et al.* Oxidative stress and deregulations in base excision repair pathway as contributors to gallbladder anomalies and carcinoma – a study involving North-East Indian population. Free Radical Research. 2019; **53**: 473–485.

5 Wang S, Su T, Tong H, Zhou D, Ma F, Ding J *et al.* Circβ-catenin promotes tumor growth and Warburg effect of gallbladder cancer by regulating STMN1 expression. Cell Death Discov. 2021; **7**. doi:10.1038/s41420-021-00626-6.

6 Shah UA, Nandikolla AG, Rajdev L. Immunotherapeutic Approaches to Biliary Cancer. Curr. Treat. Options in Oncol. 2017; **18**. doi:10.1007/s11864-017-0486-9.

7 Sędzikowska A, Szablewski L. Insulin and Insulin Resistance in Alzheimer's Disease. IJMS. 2021; **22**: 9987.

8 Zhang Y, Wang J, Liu X. LRRC19—A Bridge between Selenium Adjuvant Therapy and Renal Clear Cell Carcinoma: A Study Based on Datamining. Genes. 2020; **11**: 440.

9 Ferrucci-Da Silva C, Zhan L, Shen J, Kong B, Campbell MJ, Memon N *et al.* Effects of total parenteral nutrition on drug metabolism gene expression in mice. Acta Pharmaceutica Sinica B. 2020; **10**: 153–158.

10 Yang Z, Yang L, Zou Q, Yuan Y, Li J, Liang L *et al.* Positive ALDH1A3 and Negative GPX3 Expressions Are Biomarkers for Poor Prognosis of Gallbladder Cancer. Disease Markers. 2013; **35**: 163–172.

11 Jelic MD, Mandic AD, Maricic SM, Srdjenovic BU. Oxidative stress and its role in cancer. Journal of Cancer Research and Therapeutics. 2021; **17**: 22–28.

12 Klaunig JE. Oxidative Stress and Cancer. CPD. 2019; **24**: 4771–4778.

13 gianni. TFAP2A is a novel regulator that modulates ferroptosis in gallbladder carcinoma cells via the Nrf2 signalling axis. European Review. 2020. doi:10.26355/eurrev_202005_21163.

14 Nakagawa T, Johnson RJ, Andres-Hernando A, Roncal-Jimenez C, Sanchez-Lozada LG, Tolan DR *et al.* Fructose Production and Metabolism in the Kidney. JASN. 2020; **31**: 898–906.

15 Fila M, Chojnacki C, Chojnacki J, Blasiak J. Nutrients to Improve Mitochondrial Function to Reduce Brain Energy Deficit and Oxidative Stress in Migraine. Nutrients. 2021; **13**: 4433.

16 Li M, Thorne RF, Shi R, Zhang XD, Li J, Li J *et al.* DDIT3 Directs a Dual Mechanism to Balance Glycolysis and Oxidative Phosphorylation during Glutamine Deprivation. Advanced Science. 2021; **8**. doi:10.1002/advs.202003732.

17 Zheng L, Zhang Z, Sheng P, Mobasheri A. The role of metabolism in chondrocyte dysfunction and the progression of osteoarthritis. Ageing Research Reviews. 2021; **66**: 101249.

18 Worley BL, Kim YS, Mardini J, Zaman R, Leon KE, Vallur PG *et al.* GPx3 supports ovarian cancer progression by manipulating the extracellular redox environment. Redox Biology. 2019; **25**: 101051.

19 Wang Z, Zhu J, Liu Y, Wang Z, Cao X, Gu Y. Tumor-polarized GPX3 + AT2 lung epithelial cells promote premetastatic niche formation. Proc. Natl. Acad. Sci. U.S.A. 2022; **119**. doi:10.1073/pnas.2201899119.

20 An BC, Choi Y-D, Oh I-J, Kim JH, Park J-I, Lee S. GPx3-mediated redox signaling arrests the cell cycle and acts as a tumor suppressor in lung cancer cell lines. PLoS ONE. 2018; **13**: e0204170.

21 Hu Q, Chen J, Yang W, Xu M, Zhou J, Tan J *et al.* GPX3 expression was down-regulated but positively correlated with poor outcome in human cancers. Front. Oncol. 2023; **13**. doi:10.3389/fonc.2023.990551.

22 Steele NG, Carpenter ES, Kemp SB, Sirihorachai VR, The S, Delrosario L *et al.* Multimodal mapping of the tumor and peripheral blood immune landscape in human pancreatic cancer. Nat Cancer. 2020; **1**: 1097–1112.

23 Carpenter ES, Elhossiny AM, Kadiyala P, Li J, McGue J, Griffith BD *et al.* Analysis of Donor Pancreata Defines the Transcriptomic Signature and Microenvironment of Early Neoplastic Lesions. Cancer Discovery. 2023; **13**: 1324–1345.

24 Arunachalam D, Ramanathan SM, Menon A, Madhav L, Ramaswamy G, Namperumalsamy VP *et al.* Expression of immune response genes in human corneal epithelial cells interacting with Aspergillus flavus conidia. BMC Genomics. 2022; **23**. doi:10.1186/s12864-021-08218-5.

25 Linkner TR, Ambrus V, Kunkli B, Szojka ZI, Kalló G, Csősz É *et al.* Cellular Proteo-Transcriptomic Changes in the Immediate Early-Phase of Lentiviral Transduction. Microorganisms. 2021; **9**: 2207.

26 Satpathy S, Krug K, Jean Beltran PM, Savage SR, Petralia F, Kumar-Sinha C *et al.* A proteogenomic portrait of lung squamous cell carcinoma. Cell. 2021; **184**: 4348-4371.e40.

27 Hou J, Cao G, Tian L, Zhou R, Zhang Y, Xu H *et al.* Integrated transcriptomics and metabolomics analysis reveals that C3 and C5 are vital targets of DuZhi Wan in protecting against cerebral ischemic injury. Biomedicine & Pharmacotherapy. 2022; **155**: 113703.

28 Chi N-F, Chang T-H, Lee C-Y, Wu Y-W, Shen T-A, Chan L *et al.* Untargeted metabolomics predicts the functional outcome of ischemic stroke. Journal of the Formosan Medical Association. 2021; **120**: 234–241.

29 Jiang B-C, He L-N, Wu X-B, Shi H, Zhang W-W, Zhang Z-J *et al.* Promoted Interaction of C/EBPα with DemethylatedCxcr3Gene Promoter Contributes to Neuropathic Pain in Mice. J. Neurosci. 2016; **37**: 685–700.

30 Wang M, Liu J, Zhao Y, He R, Xu X, Guo X *et al.* Upregulation of METTL14 mediates the elevation of PERP mRNA N6 adenosine methylation promoting the growth and metastasis of pancreatic cancer. Mol Cancer. 2020; **19**. doi:10.1186/s12943-020-01249-8.

31 Charrier M, Lorant J, Contreras-Lopez R, Téjédor G, Blanquart C, Lieubeau B *et al.* Human MuStem cells repress T-cell proliferation and cytotoxicity through both paracrine and contact-dependent pathways. Stem Cell Res Ther. 2022; **13**. doi:10.1186/s13287-021-02681-3.

32 Gestermann N, Saugy D, Martignier C, Tillé L, Fuertes Marraco SA, Zettl M *et al.* LAG-3 and PD-1+LAG-3 inhibition promote anti-tumor immune responses in human autologous melanoma/T cell co-cultures. OncoImmunology. 2020; **9**. doi:10.1080/2162402x.2020.1736792.

33 Palayoor ST, Mitchell JB, Cerna D, DeGraff W, John-Aryankalayil M, Coleman CN. PX-478, an inhibitor of hypoxia-inducible factor-1α, enhances radiosensitivity of prostate carcinoma cells. Intl Journal of Cancer. 2008; **123**: 2430–2437.

34 Sun J, Shen H, Shao L, Teng X, Chen Y, Liu X *et al.* HIF-1α overexpression in mesenchymal stem cell-derived exosomes mediates cardioprotection in myocardial infarction by enhanced angiogenesis. Stem Cell Res Ther. 2020; **11**. doi:10.1186/s13287-020-01881-7.

35 Liu L, Xie D, Xie H, Huang W, Zhang J, Jin W *et al.* <p>ARHGAP10 Inhibits the Proliferation and Metastasis of CRC Cells via Blocking the Activity of RhoA/AKT Signaling Pathway</p> OTT. 2019; **Volume 12**: 11507–11516.

36 Zhang Z, Li W, Jiang D, Liu C, Lai Z. MicroRNA-139-5p inhibits cell viability, migration and invasion and suppresses tumor growth by targeting HDGF in non-small cell lung cancer. Oncol Lett. 2020. doi:10.3892/ol.2020.11296.

37 Guo S-C, Tao S-C, Yin W-J, Qi X, Yuan T, Zhang C-Q. Exosomes derived from platelet-rich plasma promote the re-epithelization of chronic cutaneous wounds via activation of YAP in a diabetic rat model. Theranostics. 2017; **7**: 81–96.

38 Bobadilla AVP, Arévalo J, Sarró E, Byrne HM, Maini PK, Carraro T *et al.* In vitro cell migration quantification method for scratch assays. J. R. Soc. Interface. 2019; **16**: 20180709.

39 Hou Y, Zhang Q, Pang W, Hou L, Liang Y, Han X *et al.* YTHDC1-mediated augmentation of miR-30d in repressing pancreatic tumorigenesis via attenuation of RUNX1-induced transcriptional activation of Warburg effect. Cell Death Differ. 2021; **28**: 3105–3124.

40 Zhao W, Zhang L, Zhang Y, Jiang Z, Lu H, Xie Y *et al.* The CDK inhibitor AT7519 inhibits human glioblastoma cell growth by inducing apoptosis, pyroptosis and cell cycle arrest. Cell Death Dis. 2023; **14**. doi:10.1038/s41419-022-05528-8.

41 Yang Y-W, Hsu PY-J. The effect of poly(d,l-lactide-co-glycolide) microparticles with polyelectrolyte self-assembled multilayer surfaces on the cross-presentation of exogenous antigens. Biomaterials. 2008; **29**: 2516–2526.

42 Li X, Shen H, Zhang M, Teissier V, Huang EE, Gao Q *et al.* Glycolytic reprogramming in macrophages and MSCs during inflammation. Front. Immunol. 2023; **14**. doi:10.3389/fimmu.2023.1199751.

43 Zhong J, Yu H, Huang C, Zhong Q, Chen Y, Xie J *et al.* Inhibition of phosphodiesterase 4 by FCPR16 protects SH-SY5Y cells against MPP+-induced decline of mitochondrial membrane potential and oxidative stress. Redox Biology. 2018; **16**: 47–58.

44 Wang Y, Song Y, Pang Y, Yu Z, Hua W, Gu Y *et al.* miR-183-5p alleviates early injury after intracerebral hemorrhage by inhibiting heme oxygenase-1 expression. Aging. 2020; **12**: 12869–12895.

45 Ye Y-Y, Mei J-W, Xiang S-S, Li H-F, Ma Q, Song X-L *et al.* MicroRNA-30a-5p inhibits gallbladder cancer cell proliferation, migration and metastasis by targeting E2F7. Cell Death Dis. 2018; **9**. doi:10.1038/s41419-018-0444-x.

46 Su X, Sun T, Li M, Xia Y, Li M, Wang D *et al.* Lkb1 aggravates diffuse large B-cell lymphoma by promoting the function of Treg cells and immune escape. J Transl Med. 2022; **20**. doi:10.1186/s12967-022-03588-0.

47 Jacoby JJ, Erez B, Korshunova MV, Williams RR, Furutani K, Takahashi O *et al.* Treatment with HIF-1α

Antagonist PX-478 Inhibits Progression and Spread of Orthotopic Human Small Cell Lung Cancer and Lung Adenocarcinoma in Mice. Journal of Thoracic Oncology. 2010; **5**: 940–949.
48 Han F, Liu W, Shi X, Yang J, Zhang X, Li Z *et al.* SOX30 Inhibits Tumor Metastasis through Attenuating Wnt-Signaling via Transcriptional and Posttranslational Regulation of β-Catenin in Lung Cancer. EBioMedicine. 2018; **31**: 253–266.
49 Wang X, Wu Y. Protective effects of autophagy inhibitor 3-methyladenine on ischemia–reperfusion-induced retinal injury. Int Ophthalmol. 2020; **40**: 1095–1101.
50 Wu C, Liu Z, Chen Z, Xu D, Chen L, Lin H *et al.* A nonferrous ferroptosis-like strategy for antioxidant inhibition–synergized nanocatalytic tumor therapeutics. Sci. Adv. 2021; **7**. doi:10.1126/sciadv.abj8833.
51 Brigelius-Flohé R, Flohé L. Regulatory Phenomena in the Glutathione Peroxidase Superfamily. Antioxidants & Redox Signaling. 2020; **33**: 498–516.
52 Jin Y-P, Hu Y-P, Wu X-S, Wu Y-S, Ye Y-Y, Li H-F *et al.* miR-143-3p targeting of ITGA6 suppresses tumour growth and angiogenesis by downregulating PLGF expression via the PI3K/AKT pathway in gallbladder carcinoma. Cell Death Dis. 2018; **9**. doi:10.1038/s41419-017-0258-2.
53 Ren S, Shao Y, Zhao X, Hong CS, Wang F, Lu X *et al.* Integration of Metabolomics and Transcriptomics Reveals Major Metabolic Pathways and Potential Biomarker Involved in Prostate Cancer. Molecular & Cellular Proteomics. 2016; **15**: 154–163.
54 Licha D, Vidali S, Aminzadeh-Gohari S, Alka O, Breitkreuz L, Kohlbacher O *et al.* Untargeted Metabolomics Reveals Molecular Effects of Ketogenic Diet on Healthy and Tumor Xenograft Mouse Models. IJMS. 2019; **20**: 3873.
55 Choi J-Y, An BC, Jung IJ, Kim JH, Lee S. MiR-921 directly downregulates GPx3 in A549 lung cancer cells. Gene. 2019; **700**: 163–167.
56 Roma-Rodrigues C, Mendes R, Baptista PV, Fernandes AR. Targeting Tumor Microenvironment for Cancer Therapy. IJMS. 2019; **20**: 840.
57 Fukushi A, Kim H-D, Chang Y-C, Kim C-H. Revisited Metabolic Control and Reprogramming Cancers by Means of the Warburg Effect in Tumor Cells. IJMS. 2022; **23**: 10037.
58 Chen L, Huang L, Gu Y, Cang W, Sun P, Xiang Y. Lactate-Lactylation Hands between Metabolic Reprogramming and Immunosuppression. IJMS. 2022; **23**: 11943.
59 Hu T, Liu H, Liang Z, Wang F, Zhou C, Zheng X *et al.* Tumor-intrinsic CD47 signal regulates glycolysis and promotes colorectal cancer cell growth and metastasis. Theranostics. 2020; **10**: 4056–4072.
60 Guo D, Tong Y, Jiang X, Meng Y, Jiang H, Du L *et al.* Aerobic glycolysis promotes tumor immune evasion by hexokinase2-mediated phosphorylation of IκBα. Cell Metabolism. 2022; **34**: 1312-1324.e6.
61 Codo AC, Davanzo GG, Monteiro L de B, de Souza GF, Muraro SP, Virgilio-da-Silva JV *et al.* Elevated Glucose Levels Favor SARS-CoV-2 Infection and Monocyte Response through a HIF-1α/Glycolysis-Dependent Axis. Cell Metabolism. 2020; **32**: 437-446.e5.
62 Willson JA, Arienti S, Sadiku P, Reyes L, Coelho P, Morrison T *et al.* Neutrophil HIF-1α stabilization is augmented by mitochondrial ROS produced via the glycerol 3-phosphate shuttle. Blood. 2022; **139**: 281–286.
63 Lee HJ, Do JH, Bae S, Yang S, Zhang X, Lee A *et al.* Immunohistochemical evidence for the over-expression of Glutathione peroxidase 3 in clear cell type ovarian adenocarcinoma. Med Oncol. 2010; **28**: 522–527.
64 Agnani D, Camacho-Vanegas O, Camacho C, Lele S, Odunsi K, Cohen S *et al.* Decreased levels of serum glutathione peroxidase 3 are associated with papillary serous ovarian cancer and disease progression. J Ovarian Res. 2011; **4**. doi:10.1186/1757-2215-4-18.
65 Chen T, Zhou Z, Peng M, Hu H, Sun R, Xu J *et al.* Glutathione peroxidase 3 is a novel clinical diagnostic biomarker and potential therapeutic target for neutrophils in rheumatoid arthritis. Arthritis Res Ther. 2023; **25**. doi:10.1186/s13075-023-03043-5.
66 Kaliaperumal R, Venkatachalam R, Nagarajan P, Sabapathy SK. Association of Serum Magnesium with Oxidative Stress in the Pathogenesis of Diabetic Cataract. Biol Trace Elem Res. 2020; **199**: 2869–2873.
67 Wang S, Yu M, Yan H, Liu J, Guo C. MiR-34a-5p Negatively Regulates Oxidative Stress on Lens Epithelial Cells by Silencing GPX3 – A Novel Target. Current Eye Research. 2022; **47**: 727–734.
68 Wu X, Liu L, Zheng Q, Ye H, Yang H, Hao H *et al.* Dihydrotanshinone I preconditions myocardium against ischemic injury via PKM2 glutathionylation sensitive to ROS. Acta Pharmaceutica Sinica B. 2023; **13**: 113–127.
69 Yoo HJ, Choi DW, Roh YJ, Lee Y-M, Lim J-H, Eo S *et al.* MsrB1-regulated GAPDH oxidation plays programmatic roles in shaping metabolic and inflammatory signatures during macrophage activation. Cell Reports. 2022; **41**: 111598.
70 Yao X, Li W, Fang D, Xiao C, Wu X, Li M *et al.* Emerging Roles of Energy Metabolism in Ferroptosis Regulation of Tumor Cells. Advanced Science. 2021; **8**. doi:10.1002/advs.202100997.

Figure Legends

Figure 1. Differential expression genes identified by RNA-seq in GBC.

Note: (A) Volcano plot of DEGs in the dataset. Red dots represent significantly upregulated genes, while blue dots represent significantly downregulated genes; (B) Heatmap of the top 50 upregulated and downregulated genes based on gene expression levels. The left dendrogram shows hierarchical clustering based on gene expression levels, and the right histogram represents the color gradient, with red indicating high expression levels and blue indicating low expression levels. The histogram above shows red bars representing GBC samples (Tumor group, n=3) and blue bars representing normal samples (Normal group, n=3); (C) PCA plot showing the differences between samples after dimensionality reduction of high-dimensional data. The x-axis represents the first principal component after PCA dimensionality reduction, and the y-axis represents the second principal component. The proportions explained by each principal component are indicated in parentheses; (D) Hierarchical clustering dendrogram and heatmap of all samples in the GSE139682 dataset analyzed using WGCNA; (E) Venn diagram showing the intersection of DEGs and genes selected by WGCNA analysis; (F) GO and KEGG enrichment analysis of the intersecting genes.

Figure 2. Differential proteins identified by proteomics in GBC.

Note: (A) Volcano plot of DEPs between the Tumor and Normal groups. Red dots represent significantly upregulated proteins, while blue dots represent significantly downregulated proteins; (B) PCA plot showing the differences between samples after dimensionality reduction of high-dimensional data. The x-axis represents the first principal component after PCA dimensionality reduction, and the y-axis represents the second principal component. The proportions explained by each principal component are indicated in parentheses; (C) Heatmap of the top 50 upregulated and downregulated proteins based on protein expression levels. The left dendrogram shows

hierarchical clustering based on protein expression levels, and the right histogram represents the color gradient, with red indicating high expression levels and blue indicating low expression levels. The histogram above shows red bars representing GBC group samples (Tumor group, n=6) and blue bars representing normal samples (Normal group, n=6); (D-E) Bar plot and bubble plot of GO and KEGG enrichment analysis of DEGs; (F) Venn diagram showing the intersection of DEGs, DEPs, genes selected by WGCNA analysis, and the GBC-related gene set in the Genecards database; (G-H) RT-qPCR and Western blot to detect the mRNA and protein levels of GPX3 in samples from each group. Six cases of normal gallbladder samples (Normal group) and six cases of GBC samples (Tumor group) were analyzed. * indicates significant difference between the two groups with $P < 0.05$.

Figure 3. Differential metabolomic analysis and enrichment analysis.

Note: (A) Volcano plot of differential metabolites, combining log2FC plot and T-test results. Red dots represent significantly upregulated metabolites, while blue dots represent significantly downregulated metabolites (Normal group: n=6; Tumor group: n=6); (B) Heatmap of differential metabolites between the two groups; (C) VIP score plot of the top 15 metabolites in the OPLS-DA analysis; (D) Venn diagram showing the intersection of differential metabolites identified in the log2FC plot, T-test plot, and OPLS-DA analysis; (E-F) Functional enrichment analysis of differential metabolites in the MetaboAnalyst database, where (E) represents the KEGG pathway analysis and (F) represents the SMPDB analysis.

Figure 4. Identification of key genes and metabolic pathways regulating GBC progression through integrated multi-omics analysis.

This figure showcases the use of RNA-sequencing, proteomics, and metabolomics to identify key molecular targets in GBC. GPX3 was identified as a critical gene linked to oxidative stress and glycolysis through an integrated analysis of DEGs, proteins, and metabolites. Blue circles indicate

downregulated entities, and red circles indicate upregulated ones. The yellow star highlights GPX3's central role. Abbreviations: GPX3 (Glutathione Peroxidase 3), DEGs (Differentially Expressed Genes), DEPs (Differentially Expressed Proteins), DEMs (Differentially Expressed Metabolites). (Created with BioRender.com)

Figure 5. Impact of GPX3 on the biological function of NOZ cell line.

Note: (A) Workflow of *in vitro* experiments; groups oe-NC and oe-GPX3 are GBC-SD cells, groups sh-NC and sh-GPX3 are NOZ cells, groups MUT-CON and GPX3-MUT are sh-GPX3 NOZ cells (Created with BioRender.com); (B-C) Cell viability and proliferation changes assessed using CCK8 and colony formation assays; (D-E) Cell migration capability assessed through scratch assay (scale bar: 100 μm) and Transwell assay (scale bar: 50 μm); (F) Cell invasion capability assessed using Transwell assay (scale bar: 50 μm); (G) Flow cytometry analysis of cell apoptosis in different groups, with statistical data of early and late apoptosis indicated in the corresponding graphs. Quantitative data are presented as mean ± standard deviation, and non-paired t-tests were used for intergroup comparisons. * indicates $P < 0.05$ compared to the control group. All cell experiments were performed in triplicate.

Figure 6. GPX3 regulation of cellular oxidative stress, glycolysis, and immune evasion.

Note: (A) Flow cytometry was used to measure the levels of ROS in each cell group; (B) Measurement of GSH/GSSG levels; (C) The levels of MDA in each cell group were detected; (D) Seahorse XFp assay was used to analyze ECAR as an indicator of mitochondrial respiration capacity; (E) Seahorse XFp assay was used to analyze OCR as an indicator of mitochondrial respiration capacity; (F) Calculated basal/maximal respiration, ATP production, spare respiratory capacity, and non-mitochondrial respiration; (G) Metabolic phenotype mapping based on OCR and ECAR; (H) The levels of glycolytic products lactate and pyruvate were measured in each cell group; (I) Example image of co-culture of GBC cell line and T cells (Created with BioRender.com);

(J) Western blot analysis was performed to measure the expression of T cell activation markers CD25, CD44, and CD69; (K) ELISA was used to measure the levels of IL-2, IFN-γ, and TNF-α in the T cell culture supernatant. Data are presented as mean ± standard deviation, and a non-paired t-test was used for comparison between groups. * indicates $P < 0.05$. All cell experiments were repeated 3 times.

Figure 7. GPX3 integrates metabolic reprogramming and immune evasion through the HIF-1α signaling pathway

Notes: (A) Western blot analysis of HIF-1α protein levels in oe-NC, oe-GPX3, sh-NC, and sh-GPX3 cells; (B) Measurement of lactate and pyruvate levels in sh-GPX3 NOZ cells following treatment with the HIF-1α inhibitor PX-478 (20 μM) for 24 hours; (C) ECAR analysis of mitochondrial respiratory activity in sh-GPX3 NOZ cells using the Seahorse XFp analyzer; (D) Representative schematic of the co-culture system of GBC cells and T cells; (E) Western blot detection of T-cell activation markers CD25, CD44, and CD69 after co-culture with sh-GPX3 NOZ cells treated with PX-478 or vehicle control; (F) ELISA quantification of IFN-γ, IL-2, and TNF-α levels in the supernatant of the above co-culture system. Data are presented as mean ± standard deviation, and a non-paired t-test was used for comparison between groups. * indicates $P < 0.05$. All cell experiments were repeated 3 times.

Figure 8. GPX3 regulation of tumor volume in mice.

Note: (A) Schematic diagram of the animal experiment procedure. oe-NC and oe-GPX3 groups were injected with GBC-SD cells, while sh-NC and sh-GPX3 groups were injected with NOZ cells (Created with BioRender.com); (B) Changes in tumor volume in each group of mice; (C) On DAY27, *in vivo* IVIS imaging was used to detect bioluminescence in mice from each group; (D) Tumor samples were collected and weighed upon euthanization of the mice. Data are presented as mean ± standard deviation, and a non-paired t-test was used for comparison between groups. *

indicates $P < 0.05$. Each group consisted of n = 5 mice.

Figure 9. The impact of GPX3 on mouse tumor metastasis and immune evasion.

Note: (A) H&E staining of xenograft tumor sections and immunohistochemical staining of fructose-2,6-bisphosphatase HK2 and cell cycle protein Ki-67 (scale bar: 100 μm); (B) Immunohistochemical staining of tumor tissue sections with 8-hydroxy-2'-deoxyguanosine (8-OHdG) (scale bar: 50 μm); (C) Measurement ofMDA content in serum; (D) ELISA detection of immune factors IL-2, IFN-γ, and TNF-α content in serum; (E) Western blot detection of GPX3, CD25, CD44, and CD69 protein expression in tumor tissue; (F) Mouse liver images and H&E stained tissue sections from each group (scale bar: 250 / 100 μm). Data are presented as mean ± standard deviation, and a non-paired t-test was used for comparison between groups. * indicates $P < 0.05$. Each group consisted of n = 5 mice.

Figure 10. *In vivo* inhibition of HIF-1α reverses GPX3-silencing–induced tumor growth and immune suppression.

Notes: (A) Schematic of the experimental design; (B) Tumor growth curves of mice during treatment (n = 5); (C) Representative IVIS bioluminescence images and quantitative analyses at the end of treatment; (D) Photographs and quantification of tumor weights after excision; (E) H&E staining and IHC staining of xenograft tumor sections for HK2 and Ki-67 (scale bar: 100 μm); (F) Western blot analysis of T-cell activation markers CD25, CD44, and CD69 in tumor lysates; (G) ELISA quantification of serum IFN-γ and TNF-α concentrations in each group. Data are presented as mean ± standard deviation, and a non-paired t-test was used for comparison between groups. * indicates $P < 0.05$. Each group consisted of n = 5 mice.

Figure 11. Downregulation of GPX3 Expression in gallbladder cancer enhances oxidative stress and glycolysis to promote immune escape and metastasis in gallbladder cancer.

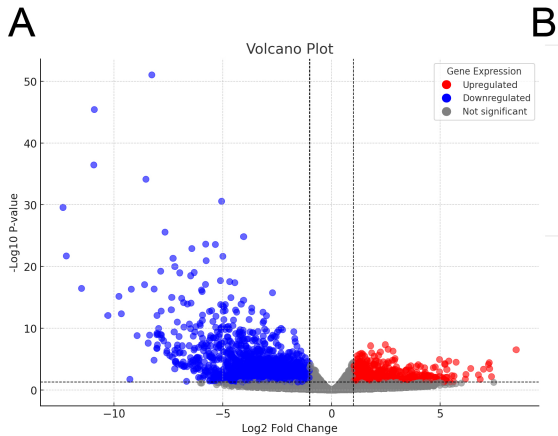
A
Volcano Plot
Gene Expression
Upregulated
Downregulated
Not significant
-Log10 P-value
Log2 Fold Change

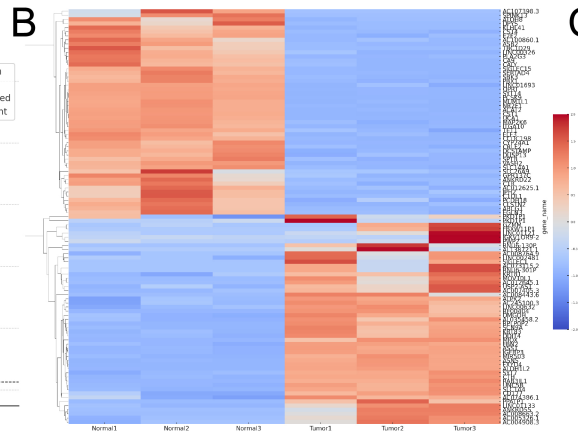
B
Normal1
Normal2
Normal3
Tumor1
Tumor2
Tumor3

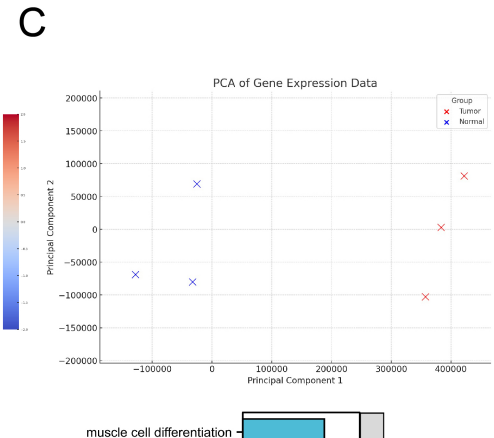
C
PCA of Gene Expression Data
Group
Tumor
Normal
Principal Component 2
Principal Component 1

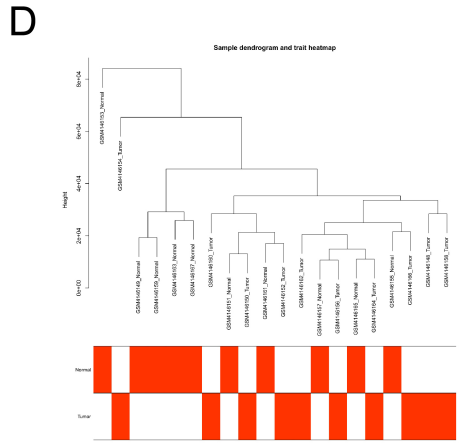
D
Sample dendrogram and trait heatmap
Height
Normal
Tumor

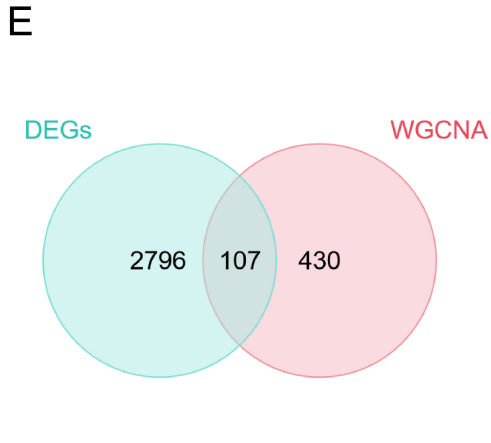
E
DEGs
WGCNA
2796
107
430

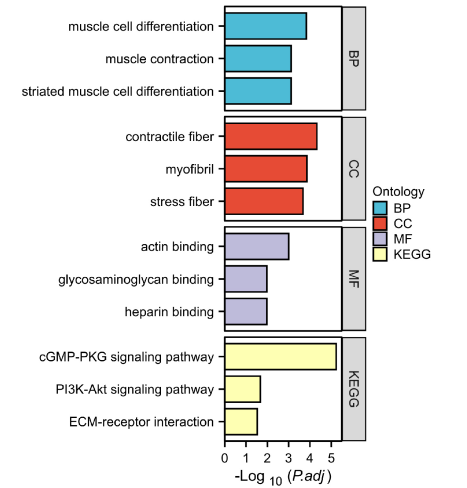
F
muscle cell differentiation
muscle contraction
striated muscle cell differentiation
BP
contractile fiber
myofibril
stress fiber
CC
actin binding
glycosaminoglycan binding
heparin binding
MF
cGMP-PKG signaling pathway
PI3K-Akt signaling pathway
ECM-receptor interaction
KEGG
Ontology
BP
CC
MF
KEGG
-Log 10 (P.adj)

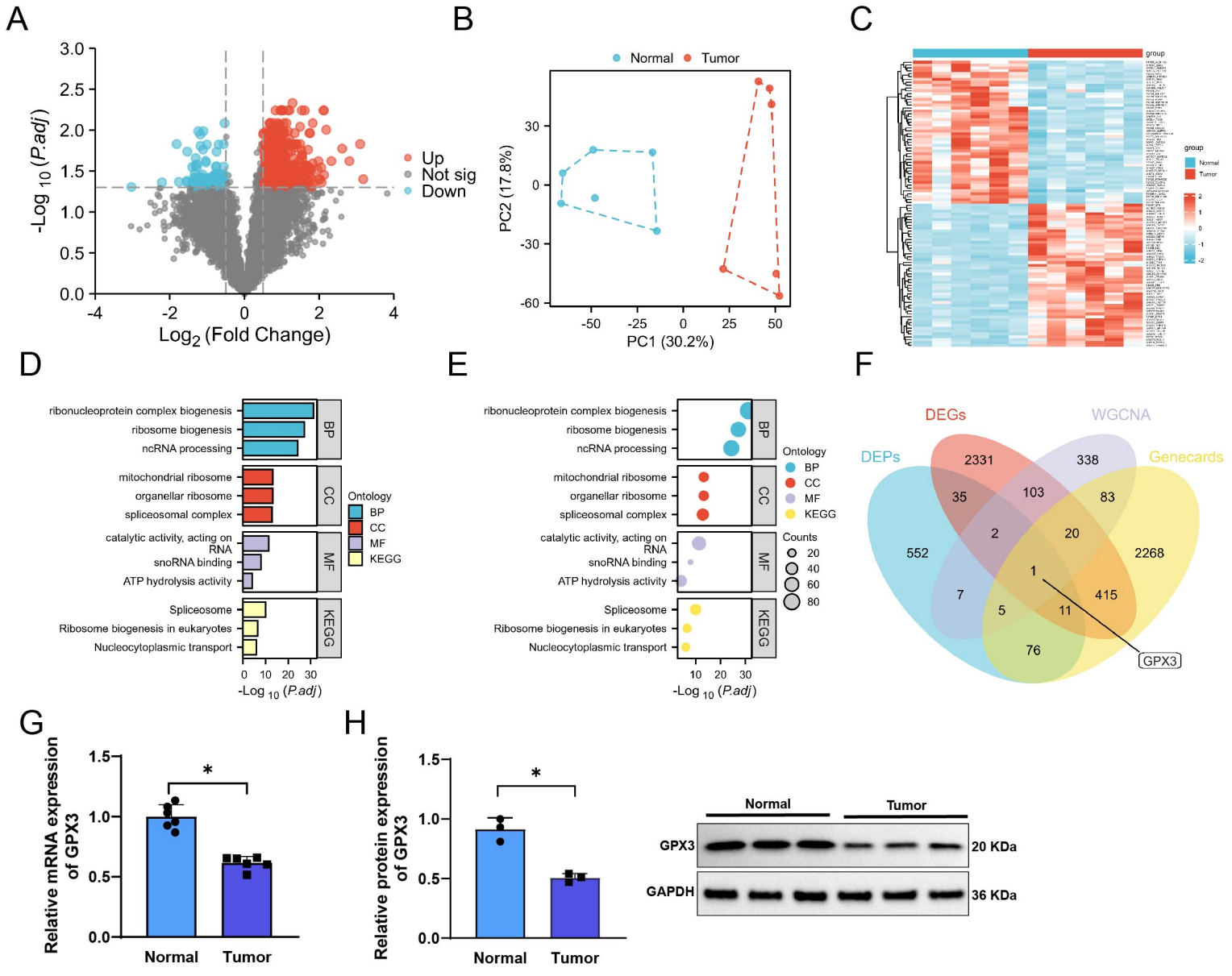
A
-Log 10 (P.adj)
Log2 (Fold Change)
Up
Not sig
Down
B
Normal
Tumor
PC2 (17.8%)
PC1 (30.2%)
C
group
Normal
Tumor
D
ribonucleoprotein complex biogenesis
ribosome biogenesis
ncRNA processing
mitochondrial ribosome
organellar ribosome
spliceosomal complex
catalytic activity, acting on RNA
snoRNA binding
ATP hydrolysis activity
Spliceosome
Ribosome biogenesis in eukaryotes
Nucleocytoplasmic transport
BP
CC
MF
KEGG
Ontology
-Log 10 (P.adj)
E
Counts
F
DEGs
WGCNA
DEPs
Genecards
2331
338
35
103
83
2
20
552
2268
1
7
415
5
11
76
GPX3
G
Relative mRNA expression of GPX3
Normal
Tumor
H
Relative protein expression of GPX3
GPX3
GAPDH
20 KDa
36 KDa

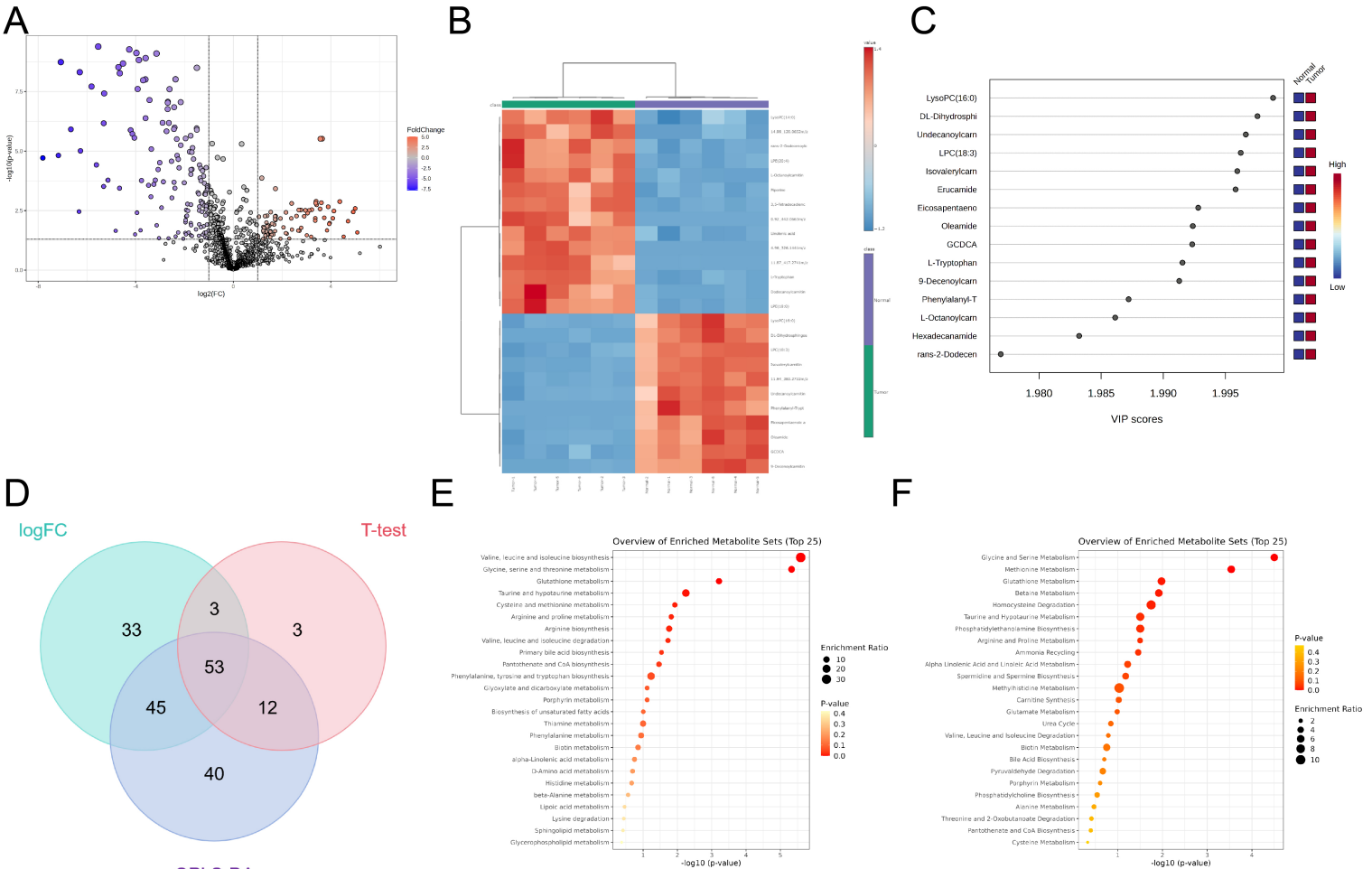
A
B
C
D
E
F
FoldChange
log2(FC)
-log10(pvalue)
LysoPC(16:0)
DL-Dihydrosphi
Undecanoylcarn
LPC(18:3)
Isovalerylcarn
Erucamide
Eicosapentaeno
Oleamide
GCDCA
L-Tryptophan
9-Decenoylcarn
Phenylalanyl-T
L-Octanoylcarn
Hexadecanamide
rans-2-Dodecen
Normal
Tumor
High
Low
VIP scores
logFC
T-test
OPLS-DA
33
3
3
53
45
12
40
Overview of Enriched Metabolite Sets (Top 25)
Valine, leucine and isoleucine biosynthesis
Glycine, serine and threonine metabolism
Glutathione metabolism
Taurine and hypotaurine metabolism
Cysteine and methionine metabolism
Arginine and proline metabolism
Arginine biosynthesis
Valine, leucine and isoleucine degradation
Primary bile acid biosynthesis
Pantothenate and CoA biosynthesis
Phenylalanine, tyrosine and tryptophan biosynthesis
Glyoxylate and dicarboxylate metabolism
Porphyrin metabolism
Biosynthesis of unsaturated fatty acids
Thiamine metabolism
Phenylalanine metabolism
Biotin metabolism
alpha-Linolenic acid metabolism
D-Amino acid metabolism
Histidine metabolism
beta-Alanine metabolism
Lipoic acid metabolism
Lysine degradation
Sphingolipid metabolism
Glycerophospholipid metabolism
-log10 (p-value)
Enrichment Ratio
P-value
Overview of Enriched Metabolite Sets (Top 25)
Glycine and Serine Metabolism
Methionine Metabolism
Glutathione Metabolism
Betaine Metabolism
Homocysteine Degradation
Taurine and Hypotaurine Metabolism
Phosphatidylethanolamine Biosynthesis
Arginine and Proline Metabolism
Ammonia Recycling
Alpha Linolenic Acid and Linoleic Acid Metabolism
Spermidine and Spermine Biosynthesis
Methylhistidine Metabolism
Carnitine Synthesis
Glutamate Metabolism
Urea Cycle
Valine, Leucine and Isoleucine Degradation
Biotin Metabolism
Bile Acid Biosynthesis
Pyruvaldehyde Degradation
Porphyrin Metabolism
Phosphatidylcholine Biosynthesis
Alanine Metabolism
Threonine and 2-Oxobutanoate Degradation
Pantothenate and CoA Biosynthesis
Cysteine Metabolism
-log10 (p-value)
P-value
Enrichment Ratio

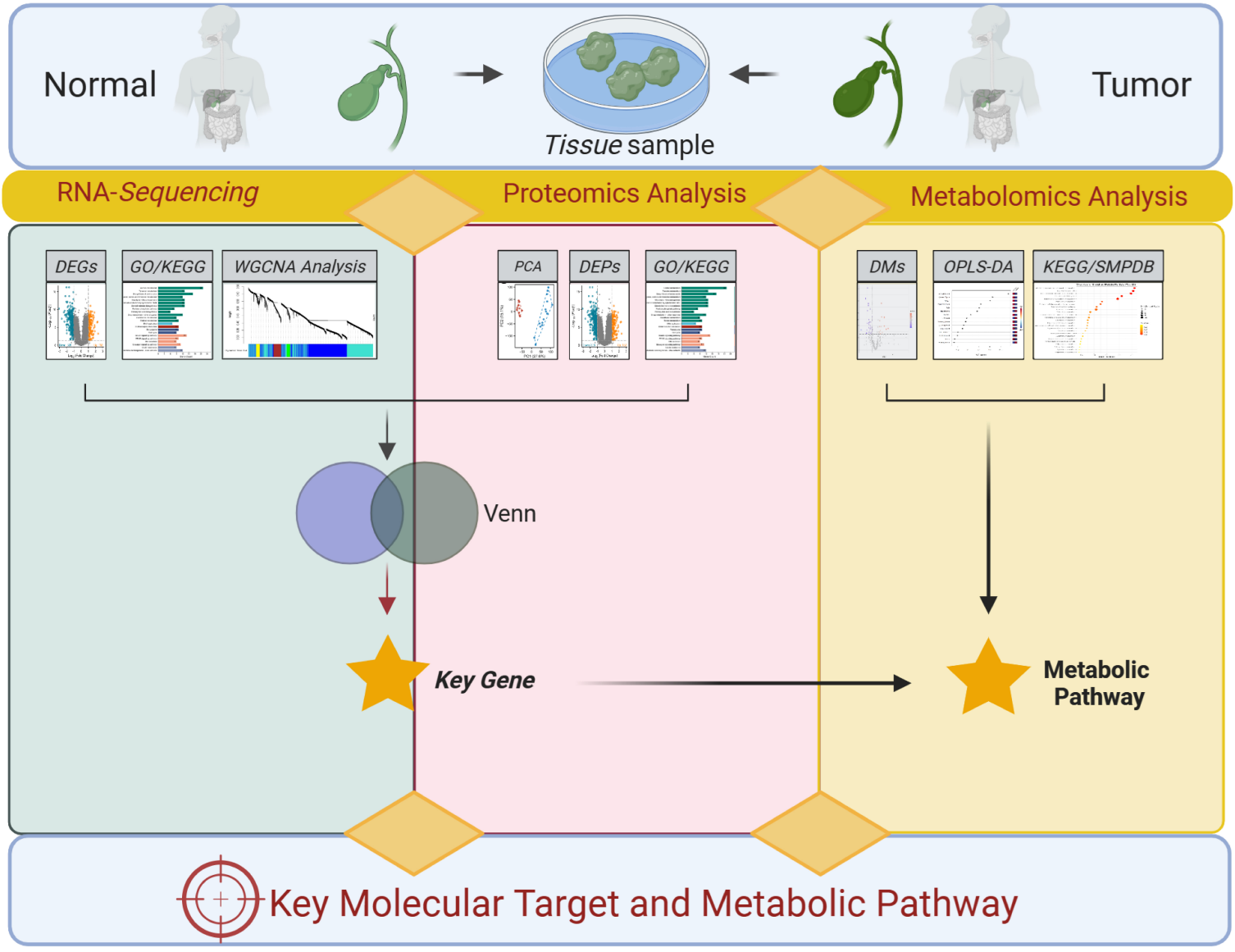
Normal
Tumor
Tissue sample
RNA-Sequencing
Proteomics Analysis
Metabolomics Analysis
DEGs
GO/KEGG
WGCNA Analysis
PCA
DEPs
GO/KEGG
DMs
OPLS-DA
KEGG/SMPDB
Venn
Key Gene
Metabolic Pathway
Key Molecular Target and Metabolic Pathway

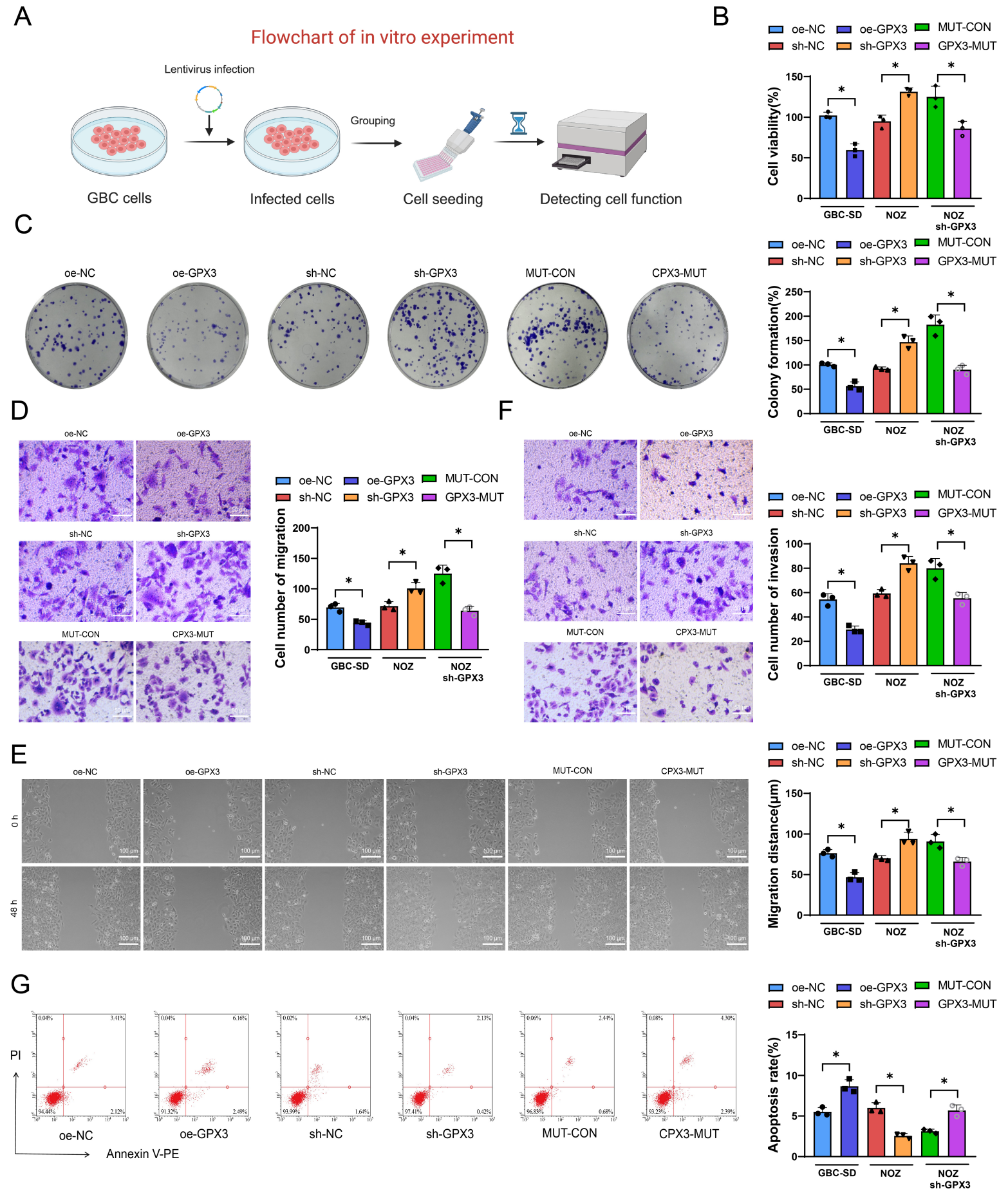
A
Flowchart of in vitro experiment
Lentivirus infection
Grouping
GBC cells
Infected cells
Cell seeding
Detecting cell function
B
oe-NC
oe-GPX3
sh-NC
sh-GPX3
MUT-CON
GPX3-MUT
Cell viability(%)
GBC-SD
NOZ
NOZ sh-GPX3
C
oe-NC
oe-GPX3
sh-NC
sh-GPX3
MUT-CON
CPX3-MUT
Colony formation(%)
D
Cell number of migration
F
Cell number of invasion
E
0 h
48 h
Migration distance(μm)
G
PI
Annexin V-PE
Apoptosis rate(%)

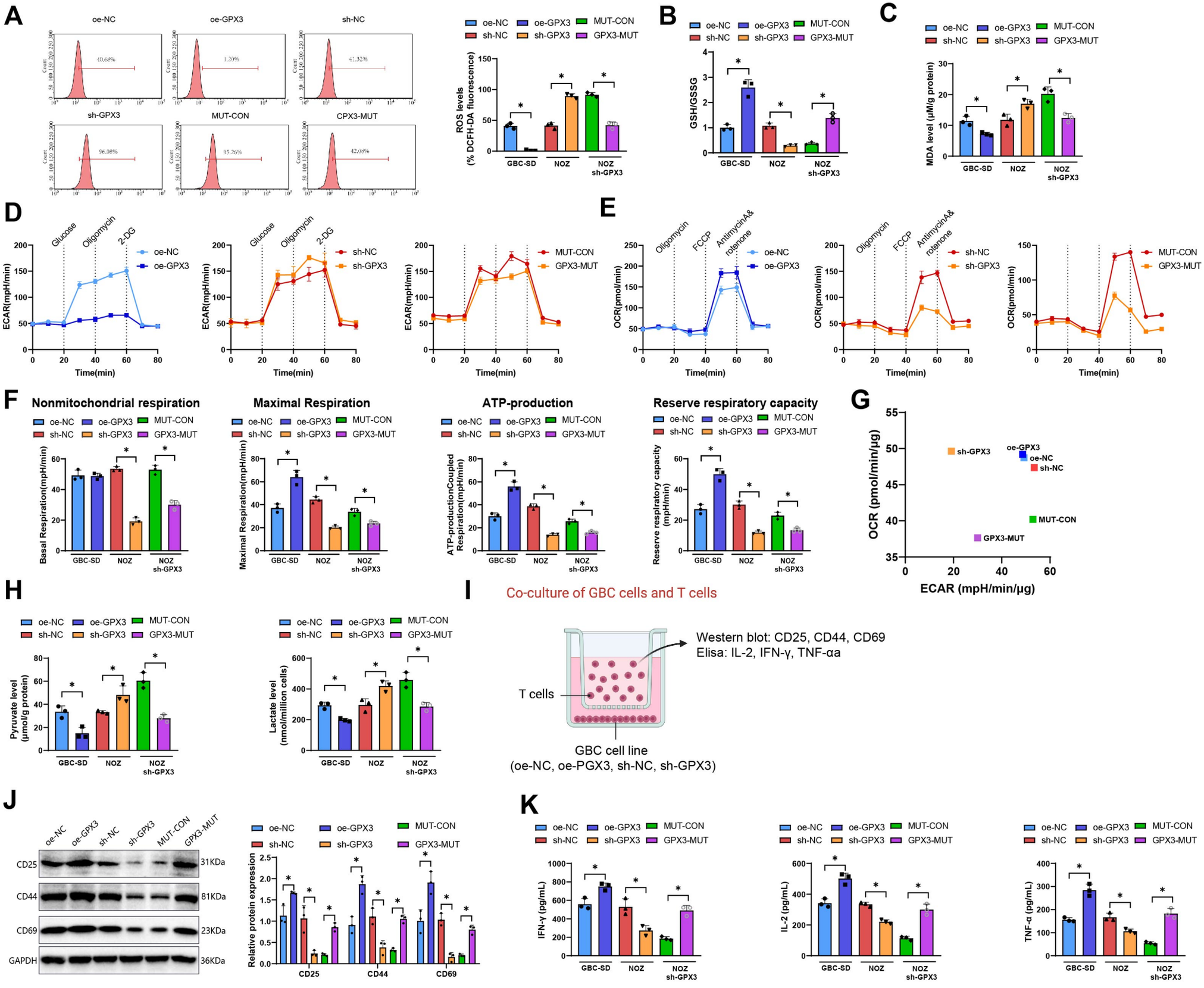
A
oe-NC
oe-GPX3
sh-NC
sh-GPX3
MUT-CON
CPX3-MUT
40.68%
1.20%
41.32%
96.08%
95.26%
42.08%
Count
oe-NC oe-GPX3 MUT-CON
sh-NC sh-GPX3 GPX3-MUT
ROS levels (% DCFH-DA fluorescence)
B
GSH/GSSG
C
MDA level (μM/g protein)
GBC-SD
NOZ
NOZ sh-GPX3
D
Glucose
Oligomycin
2-DG
ECAR(mpH/min)
Time(min)
E
Oligomycin
FCCP
AntimycinA& rotenone
OCR(pmol/min)
F
Nonmitochondrial respiration
Maximal Respiration
ATP-production
Reserve respiratory capacity
Basal Respiration(mpH/min)
Maximal Respiration(mpH/min)
ATP-productionCoupled Respiration(mpH/min)
Reserve respiratory capacity (mpH/min)
G
OCR (pmol/min/μg)
ECAR (mpH/min/μg)
H
Pyruvate level (μmol/g protein)
Lactate level (nmol/million cells)
I
Co-culture of GBC cells and T cells
Western blot: CD25, CD44, CD69
Elisa: IL-2, IFN-γ, TNF-αa
T cells
GBC cell line
(oe-NC, oe-PGX3, sh-NC, sh-GPX3)
J
CD25
CD44
CD69
GAPDH
31KDa
81KDa
23KDa
36KDa
Relative protein expression
K
IFN-γ (pg/mL)
IL-2 (pg/mL)
TNF-α (pg/mL)

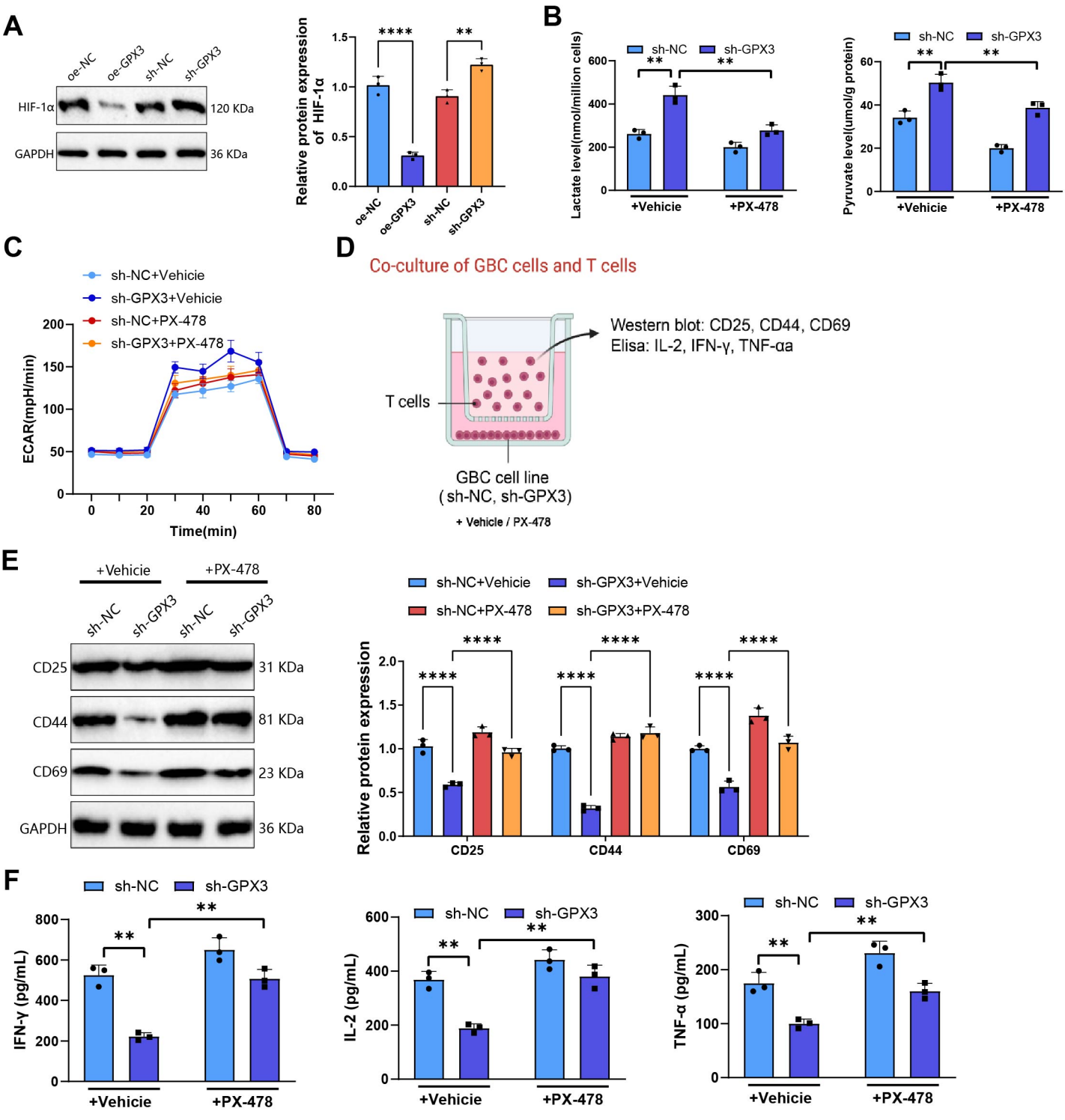
A
oe-NC
oe-GPX3
sh-NC
sh-GPX3
HIF-1α
120 KDa
GAPDH
36 KDa
Relative protein expression of HIF-1α
****
**
B
sh-NC
sh-GPX3
Lactate level(nmol/million cells)
+Vehicie
+PX-478
Pyruvate level(umol/g protein)
C
sh-NC+Vehicie
sh-GPX3+Vehicie
sh-NC+PX-478
sh-GPX3+PX-478
ECAR(mpH/min)
Time(min)
D
Co-culture of GBC cells and T cells
T cells
GBC cell line
(sh-NC, sh-GPX3)
+ Vehicle / PX-478
Western blot: CD25, CD44, CD69
Elisa: IL-2, IFN-γ, TNF-αa
E
+Vehicie
+PX-478
CD25
31 KDa
CD44
81 KDa
CD69
23 KDa
GAPDH
36 KDa
Relative protein expression
F
IFN-γ (pg/mL)
IL-2 (pg/mL)
TNF-α (pg/mL)

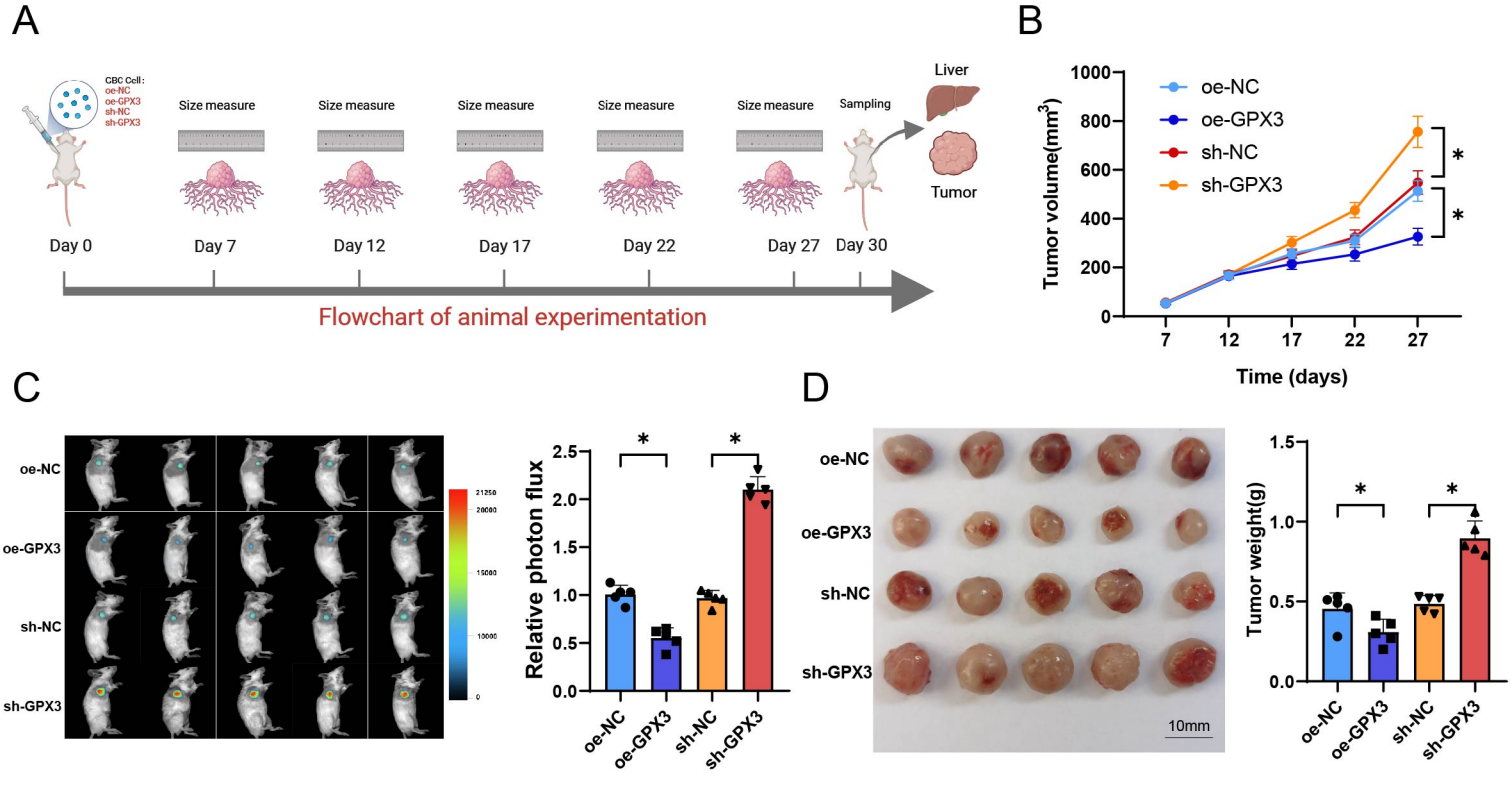
A
CBC Cell:
oe-NC
oe-GPX3
sh-NC
sh-GPX3
Size measure
Size measure
Size measure
Size measure
Size measure
Sampling
Liver
Tumor
Day 0
Day 7
Day 12
Day 17
Day 22
Day 27
Day 30
Flowchart of animal experimentation
B
Tumor volume(mm3)
1000
800
600
400
200
0
oe-NC
oe-GPX3
sh-NC
sh-GPX3
*
*
7
12
17
22
27
Time (days)
C
oe-NC
oe-GPX3
sh-NC
sh-GPX3
21250
20000
15000
10000
0
Relative photon flux
2.5
2.0
1.5
1.0
0.5
0.0
*
*
oe-NC
oe-GPX3
sh-NC
sh-GPX3
D
oe-NC
oe-GPX3
sh-NC
sh-GPX3
10mm
Tumor weight(g)
1.5
1.0
0.5
0.0
*
*
oe-NC
oe-GPX3
sh-NC
sh-GPX3

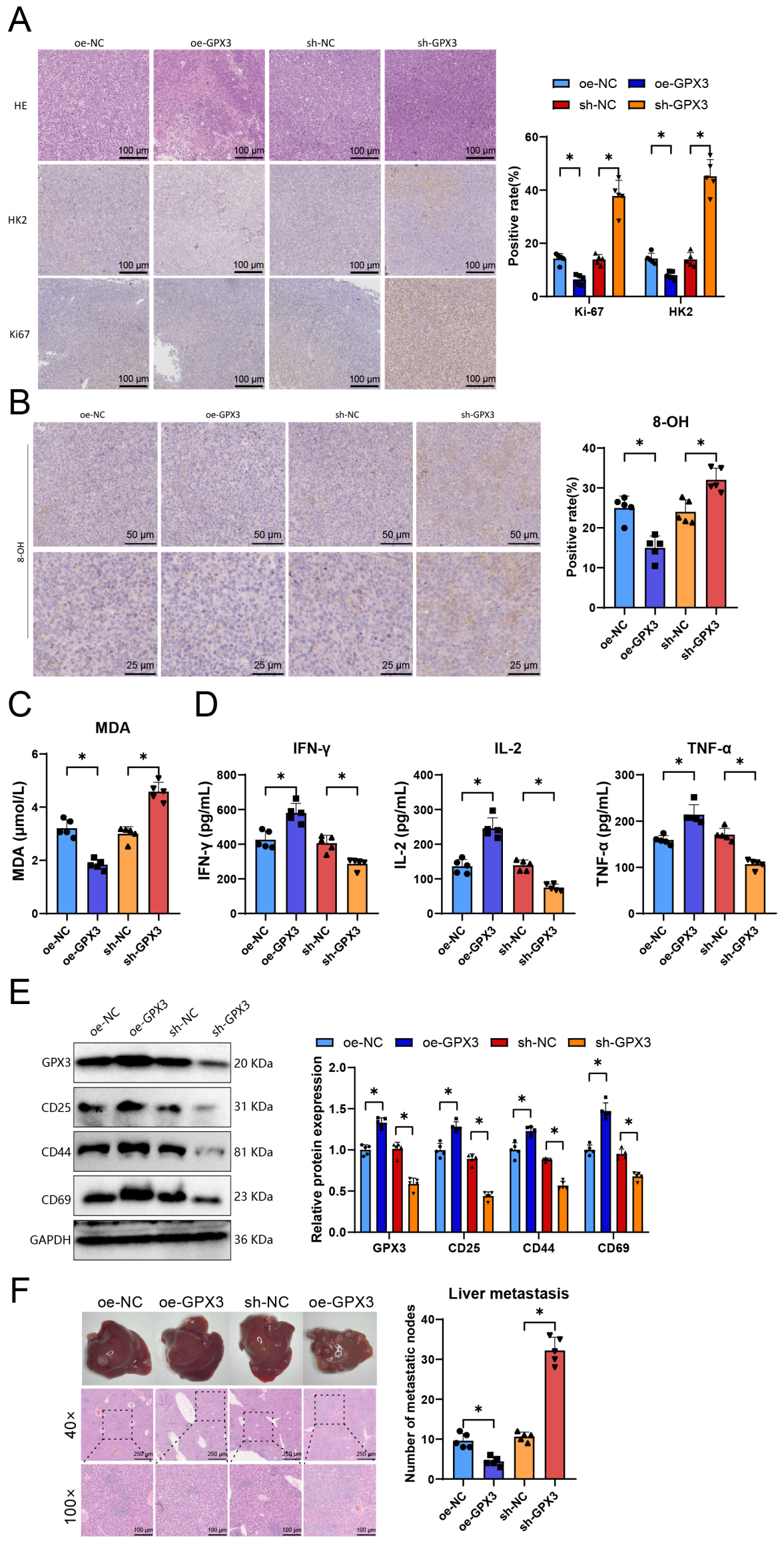
A
oe-NC
oe-GPX3
sh-NC
sh-GPX3
HE
HK2
Ki67
100 μm
Positive rate(%)
Ki-67
HK2
B
8-OH
50 μm
25 μm
C
MDA
MDA (μmol/L)
D
IFN-γ
IFN-γ (pg/mL)
IL-2
IL-2 (pg/mL)
TNF-α
TNF-α (pg/mL)
E
GPX3
CD25
CD44
CD69
GAPDH
20 KDa
31 KDa
81 KDa
23 KDa
36 KDa
Relative protein exepression
F
Liver metastasis
Number of metastatic nodes
40×
100×

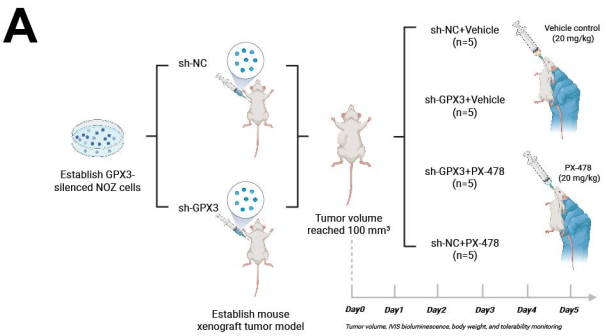
A
sh-NC
sh-GPX3
Establish GPX3-silenced NOZ cells
Establish mouse xenograft tumor model
Tumor volume reached 100 mm³
sh-NC+Vehicle (n=5)
sh-GPX3+Vehicle (n=5)
sh-GPX3+PX-478 (n=5)
sh-NC+PX-478 (n=5)
Vehicle control (20 mg/kg)
PX-478 (20 mg/kg)
Day0 Day1 Day2 Day3 Day4 Day5
Tumor volume, IVIS bioluminescence, body weight, and tolerability monitoring

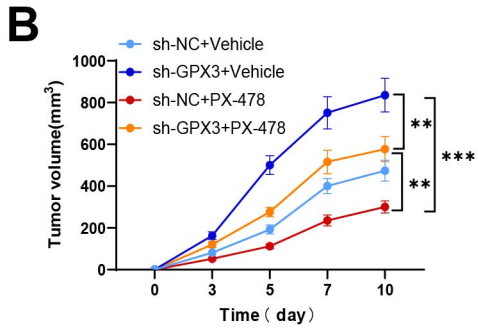
B
sh-NC+Vehicle
sh-GPX3+Vehicle
sh-NC+PX-478
sh-GPX3+PX-478
Tumor volume(mm³)
Time（day）
**
***
**

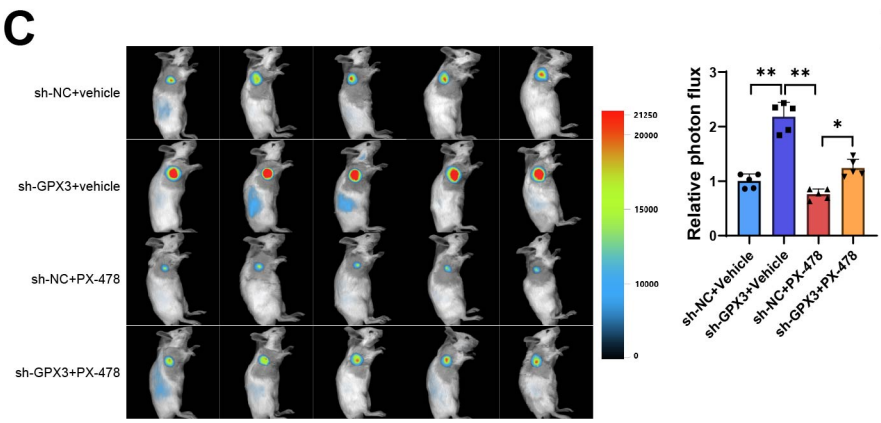
C
sh-NC+vehicle
sh-GPX3+vehicle
sh-NC+PX-478
sh-GPX3+PX-478
Relative photon flux
sh-NC+Vehicle
sh-GPX3+Vehicle
sh-NC+PX-478
sh-GPX3+PX-478

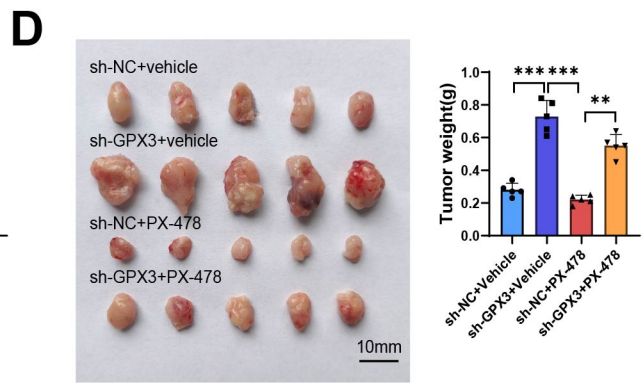
D
sh-NC+vehicle
sh-GPX3+vehicle
sh-NC+PX-478
sh-GPX3+PX-478
10mm
Tumor weight(g)

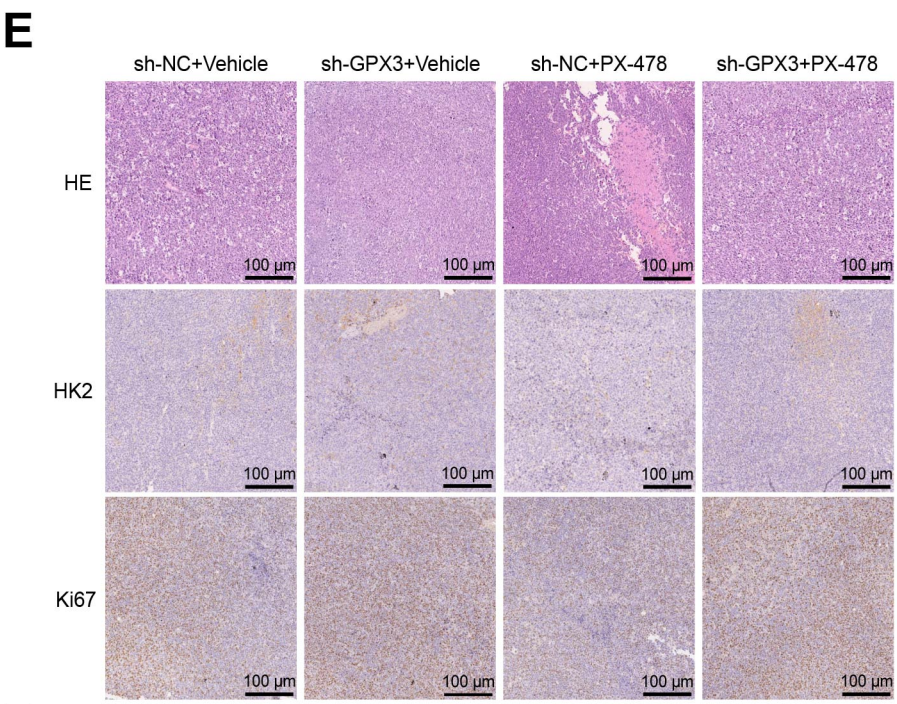
E
sh-NC+Vehicle
sh-GPX3+Vehicle
sh-NC+PX-478
sh-GPX3+PX-478
HE
HK2
Ki67
100 μm
Positive rate(%)
HK2
Ki67

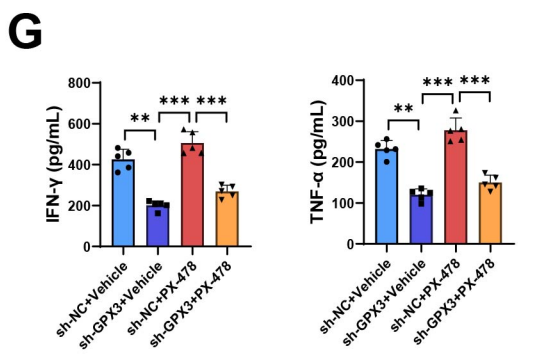
G
IFN-γ (pg/mL)
TNF-α (pg/mL)
sh-NC+Vehicle
sh-GPX3+Vehicle
sh-NC+PX-478
sh-GPX3+PX-478

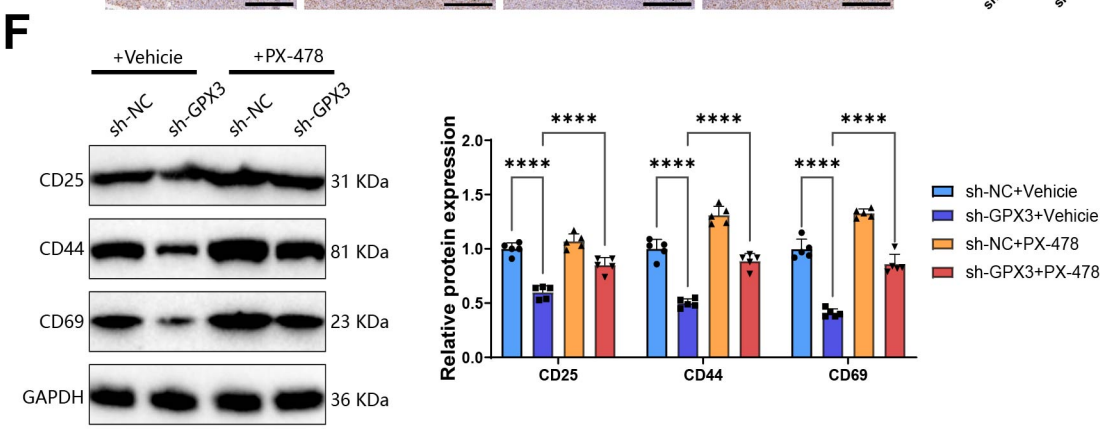
F
+Vehicie
+PX-478
sh-NC
sh-GPX3
CD25
CD44
CD69
GAPDH
31 KDa
81 KDa
23 KDa
36 KDa
Relative protein expression
sh-NC+Vehicie
sh-GPX3+Vehicie
sh-NC+PX-478
sh-GPX3+PX-478

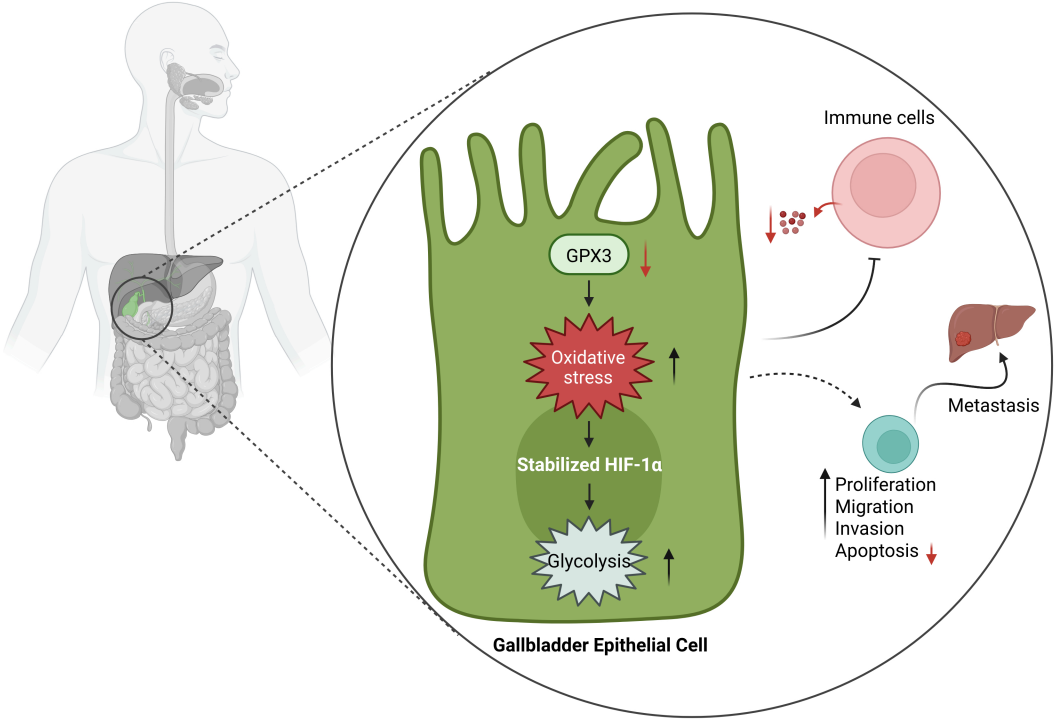
Immune cells
GPX3
Oxidative stress
Stabilized HIF-1α
Glycolysis
Gallbladder Epithelial Cell
Metastasis
Proliferation
Migration
Invasion
Apoptosis